2021

QUARK ENERGY LOSS MEASUREMENT WITH THE CLAS DETECTOR

ILHA MACHADO, GABRIELA HAMILTON

UNIVERSIDAD TÉCNICA FEDERICO SANTA MARÍA
DEPARTAMENTO DE FÍSICA
VALPARAÍSO - CHILE

EX UMBRA IN SOLEM

Quark energy loss measurement with the CLAS detector

Gabriela Hamilton Ilha Machado

Contents

Ackowledgements

I would like to thank first the person that made this all possible, Will Brooks. He was not only my advisor but a mentor to me. I am beyond grateful and words are not enough to express it. I learned from him more than I have from anyone else in physics, not only about the science itself but also what it means to be a particle physicist, or better, an **experimental** particle physicist. He was the reason I was able to move to Chile to do my Masters, always helping me in any way he could and being there in my most difficult times. During this time I met a lot of wonderful people that I have to thank too. Hayk Hakobyan, Taisiya Mineeva and Orlando Soto helped me immensely in my project, from the physics side of things and also the programming and ROOT side, specially in the beginning, when I had no idea what I was doing. Antonio, Sebastián, Andrés y Estebán, my fellow EG2 colleagues, also helped me whenever they could, with tips about the project itself but also with entertainment outside our "office hours". Antonio deserves special thanks. He helped me and still helps me so much outside of the University too. I hope we talk about video games and food from wherever I end up being in the world. Thanks to my CCTVal friends: Pablo, Benjamín and David and everyone from the Mirrors Project and SiLab. Last but not least I thank my parents, Marco Aurelio and Andréa, and my sister Anelisa, you are responsible for who I am today, my old friends Bira and Julhianna and, towards the end of the thesis, João Pedro. Even being physically apart for the most part of it, I could always find support in you and you convinced me that I was capable of doing this even when I couldn't believe it myself.

Abstract

In this analysis, we studied quark energy loss for positive pions produced in DIS events. The analysis used data from experiments carried out during the run period EG2 in Hall B of Jefferson Lab, Virginia. The experiments used a 5.014 GeV electron beam and studied the nuclear targets deuterium, carbon, iron and lead.

This phenomenon has been studied indirectly in various types of scattering experiments such as heavy-ion collisions, DIS, among others, measuring different kinds of hadrons, such as pions and kaons.

By looking at the production of π^+ from two different targets we can obtain information about quark energy loss by comparing the curves of the energy spectra. Assuming that the energy distributions from the different targets have approximately the same behaviour, the goal of the study is to measure the size of the horizontal shift between the distributions that would correspond to a shift in quark energy.

To extract quark energy loss, the method proposed is to shift the energy spectrum from the solid target by some chosen amount and compare this new distribution with the original energy spectrum from the deuterium target. To compare the curves the Kolmogorov-Smirnov statistical test was used, that gives the probability that both curves follow the same underlying distribution. If the described steps are repeated for a sufficient number of different shifts in energy a probability curve is obtained and the average energy loss can be estimated.

Chapter 1

Physics Motivation

High energy physics experiments study the microscopic structure of nuclear matter. Deep inelastic scattering (DIS) of a lepton off a nucleon is a type of particle experiment that serves as an excellent tool for studies of hadron formation processes inside a nuclear medium. The present work is a study about quark energy loss with a DIS experiment and it is presented in the following way. It starts by presenting the theoretical motivation for the analysis and what is intended to extract and observe. Then the experiment used for the analysis is described followed by a description of the analysis method used for the measurement of quark energy loss and the results of the analysis.

The physics motivation section is divided in five parts. It starts with a brief history of particle physics followed by a description of the most important features of QCD. After that is presented a brief summary of DIS and hadronization and their relation to the theme of this work. It ends with the main topic of this work, quark energy loss.

1.1 The Standard Model: A brief history of Particle Physics

When trying to understand the fundamental laws of the universe it was only a matter of time until humans started to think about matter itself. At some point came the idea that all matter in the universe can only be divided so much. This inspired the atomic theory, where the atoms of different elements could be combined and create all we see in the universe. The first particle to be discovered was the electron in 1897 by J. J. Thomson with his cathode rays experiment [1]. After that, in 1913, the Rutherford-Bohr model of the atom showed that the atoms were not truly indivisible but were made of not only electrons but protons too [2] and these were considered the new elementary particles (also known as fundamental).

Around 1930 new fundamental particles started to be discovered with cosmic rays and reactors. Eventually these experiments evolved to the particle accelerators we know today. With time we came to discover so many supposedly elemental particles that we had to think about the possibility that maybe these weren't indivisible and had their own structure.

And then the Quark Model came into existence. Independently proposed by Murray Gell-Mann [3] and George Zweig [4], it poses that the observed baryons and mesons were made of only three elementary particles, called quarks, and their corresponding antiparticles. We call the different varieties of quarks "flavors" and today we know that there are six of them: up, down, strange, charm, bottom and top. The theory also proposes that quarks have a quantum number referred to as color and that only neutral color objects can be observed as real particles. So single quarks are not observable, only bound states of specific combinations of quarks and/or antiquarks with specific colors and anticolors, which are called hadrons. There are two types of hadrons: quark-antiquark pairs are called mesons and bound states of three quarks or antiquarks are called baryons (Fig. 1.1).

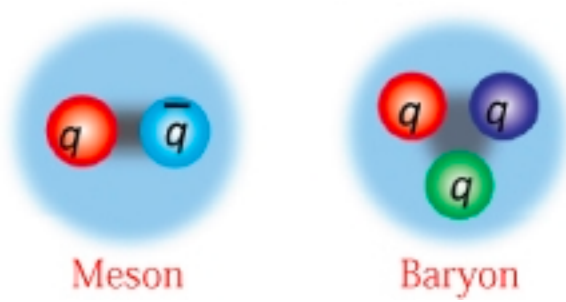

Figure 1.1: The two kinds of hadrons, a schematic of mesons and baryons.

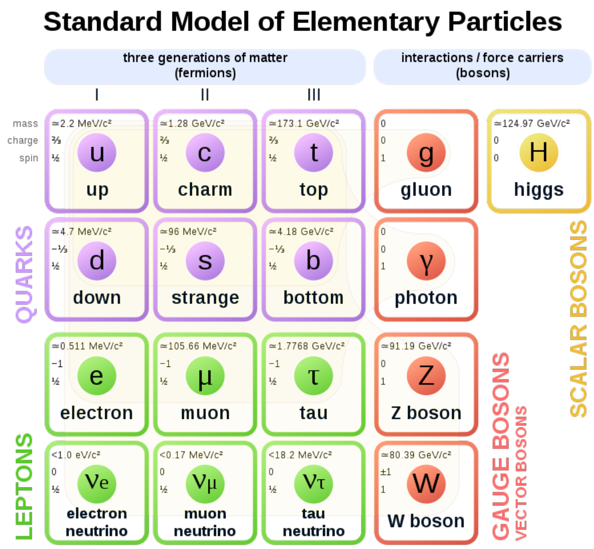

Figure 1.2: The Standard Model Elementary Particles. Image from Wikimedia Commons. Attribution: MissMJ

But quarks are not the only fundamental particles. There is a set of elementary particles called leptons. Those are the electron, muon and tau particles and three neutrinos, one for each flavor (electron neutrino, muon neutrino and tau neutrino). The leptons electron, muon and tau have electric charge but no color while the neutrinos do not have electric charge. Together with the quarks, they complete the known Fermions (particles of spin 1/2). Fig. 1.2 shows the known Quarks and Leptons.

Together with the elementary bosons, this completes the list of known Standard Model elementary particles but we also need to understand how the interactions between them work. Theories were formulated to explain these fundamental interactions or the four fundamental forces. Of these four, gravitation remains unexplained in terms of quantum theories and is not included in the SM. The other three are the well known electromagnetic force and the nuclear forces: the weak and the strong nuclear interactions.

1.2 Quantum Chromodynamics

The quark model solved a lot of problems with the introduction of quarks, but it didn't explain well enough the dynamics between them. Feynman proposed that protons had internal structure and started the formulation of the parton model [5]. This theory was applied to different scattering experiments and paved the way for the formulation of Quantum Chromodynamics.

The most successful quantum field theories are the gauge theories, in which particles of integer spin, called bosons, act as mediators of the interactions. The set of vector bosons that are reponsible for the four interactions are shown in Fig. 1.2. Quantum Chromodynamics (QCD) is an SU(3) gauge theory that explains the interaction between quarks, often referred to as the Strong interaction while the Quantum Electrodynamics theory explains the interactions of electrically charged particles.

Just like the photon is the mediator particle of QED, in QCD there is the gluon. But there are a few differences between these two theories that result in a different behavior for particles with color charge. QCD has two main features that QED does not have: asymptotic freedom and color confinement.

According to QCD the potential energy between two colored objects is weak at small relative distances, this is called asymptotic freedom. At large distances it grows strongly with separation, so colored objects (like quarks) are not observed in experiments, they are confined. These concepts are deeply linked to the behavior of the QCD coupling constant. Different from other types of interactions, the strong coupling is not constant. For low energies, or larger distances, the coupling has its highest values while for hard interactions, high energy and small distance scales, it becomes asymptotically small.

1.3 Deep Inelastic Scattering

Since the beginning of particle physics we use scattering experiments to probe the structure of matter. Rutherford used alpha particles scattered from gold to probe the structure of atoms and now we use high energy electrons to probe even smaller structures.

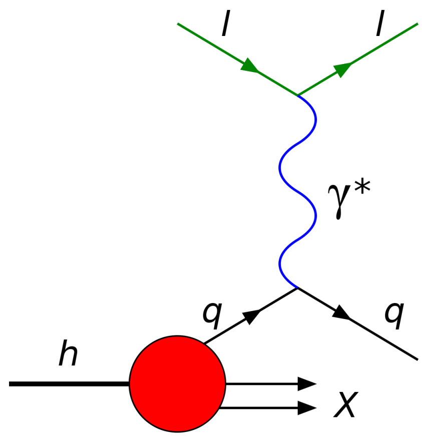

Figure 1.3: Deep inelastic scattering diagram

One of the motivations of this work is to contribute to the understanding of the process of formation of hadrons, the hadronization process. One way to study hadronization is to perturb the nuclear environment and compare the properties of final states produced on nuclei of different sizes. Deep Inelastic Scattering (DIS) is one of the many ways of doing that.

In a Deep Inelastic Scattering process a beam of leptons $l(k)$ with four-momentum k scatters off a nucleon target $h(p)$ of four-momentum p resulting in a hadronic final state X and can be represented by $l(k)+h(p) \to l'(k')+X$. A diagram of a typical DIS process can be seen in Fig. 1.3. In CLAS kinematics, the energy of the lepton beam (5 GeV) is very low so, although exchange of Z and W bosons do occur at JLab energies the probability per event is low, therefore the weak interaction can be neglected. If the interaction is assumed to be of one photon and the energy and momentum k' of the scattered electron is measured, we can characterize the virtual photon $\gamma*$ of four-momentum q, which will also be the transferred four-momentum:

$$q = k - k' \tag{1.1}$$

and the virtuality of the photon:

$$Q^2 \approx 4E_k E_{k'} sin^2(\frac{\theta}{2}) \tag{1.2}$$

$$-q^2 = Q^2 \tag{1.3}$$

The energy transfer from the electron to the nucleon is ν:

$$\nu = \frac{p \cdot q}{M} \tag{1.4}$$

or $\nu = E_k - E_{k'}$ in the target rest frame.

The DIS process is called "Deep" because it is a scattering of highly energetic particles off a hadron, resulting in a photon of high virtuality allowing us to take a "look" at distance scales smaller than that of the target nucleus, probing its structure. The resolution necessary to resolve a parton is around 0.2 fm, that corresponds to the kinematic region with $Q^2 > 1$ GeV^2. DIS is also "Inelastic" because the invariant mass of the hadronic final state X is much larger than that of a nucleon. The squared mass of the total hadronic system is $M_x^2 \equiv W^2$ where:

$$W^2 = (p+q)^2 = M^2 + 2M\nu - Q^2 \tag{1.5}$$

with M as the mass of the target. The scattering is elastic when $M^2 = W^2$ and thus $2M\nu - Q^2 = 0$. To also isolate DIS from resonance production and the diffractive regime, the mass of the final states must exceed the hadronic resonances so it's required that $W^2 > 2$ GeV.

Other useful variables include the Bjorken scaling variable:

$$x = \frac{Q^2}{2M\nu} \tag{1.6}$$

with its value being 1 for elastic scatterings and $0 < x < 1$ for inelastic scatterings and the fractional energy y of the virtual photon:

$$y = \frac{p \cdot q}{p \cdot k} \tag{1.7}$$

or $y = \dfrac{\nu}{E_k}$ in the target rest frame.

For inclusive DIS only the scattered lepton is detected while for Semi-Inclusive DIS (SIDIS) an additional final-state hadron is detected. SIDIS is particularly interesting because the four-momentum of the detected hadron p_h provides information about the struck quark. In this case one can also define a variable for the fraction of the energy of the virtual photon transferred to the produced hadron as:

$$z = \frac{p \cdot p_h}{p \cdot q} \tag{1.8}$$

or $z = \dfrac{E_h}{\nu}$ in the target rest frame, where E_h is the energy of the hadron. The transverse momentum p_T of the hadron is with respect to the direction of the virtual photon γ^*. The ϕ_h is defined as the angle between the leptonic and hadronic planes.

1.4 Hadronization

In DIS, the incoming electron, if it has enough energy, interacts directly with a valence quark of the nucleon through a virtual photon. The valence quark is "kicked out" of the nucleon but it cannot be observed in its single colored state, so it has to hadronize, meaning it has to become a hadron so it complies with color confinement. Hadronization refers to the process that the quark goes through in order to become a hadron. The experimental data used in this work is from a SIDIS experiment, where the scattered electron and some of the resulting hadrons are measured, since one of the goals is to contribute to the study of hadronization processes.

The Lund String Model [6] was originally developed by members of the Department of Theoretical Physics at Lund University and is a well-established model for the hadronization process. The quarks that make up the hadron are connected by a gluon field so, in this model, the field lines are as if it were like a massless string tying the quarks together. If you try to separate them the string stretches and stores more energy. At some point, if you keep separating them, the energy stored becomes large enough to create a quark-antiquark pair and the string breaks. The model was inspired by the asymptotic freedom and confinement concepts.

This Lund String Model has been implemented in the PYTHIA [7] event generator, one of the most widely used Monte Carlo generators for pp collisions at high energies. Fig. 1.4 shows a visual representation of lattice QCD simulations of the flux tubes for a meson and a baryon.

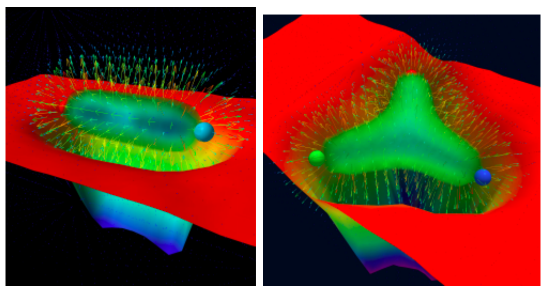

Figure 1.4: Lattice QCD simulations for a meson and a baryon from http://www.physics.adelaide.edu.au/theory/staff/leinweber/VisualQCD/Nobel/index.html

1.4.1 Hadronization in a nuclear environment

There are other effects that have to be taken into consideration when the hadronization occurs in a medium and not "in a vacuum". In a medium, like a nuclear environment, there are plenty more partons for the scattered quark to interact with. The EG2 data is precisely of this kind. In this case the nuclear media tested in the experiment, or "cold QCD matter", are the nuclear targets themselves: carbon (C), iron (Fe) and lead (Pb). When the quark is scattered and goes into the nuclear medium while hadronizing it can interact with other partons and in turn lose energy. This is precisely the main topic of this work, so this subject will be further developed in the next section.

1.5 Quark Energy Loss

1.5.1 QED Bremsstrahlung and LPM effect

Energy loss in this context is a very simple concept that is accurately self-descriptive since it is about how much energy a particle loses when passing through a medium. But not only quarks lose energy in a medium, charged leptons can also lose energy, although quark energy loss is caused by strong interactions while leptons lose energy vie electromagnetic interactions. A very well known mechanism for this kind of energy loss is bremsstrahlung radiation: the radiated energy from an electrically charged particle interacting with another charged particle (or scattering site), let's say, a muon interacting with a nucleon. The picture below (Fig. 1.5) shows how much energy a muon loses when going through a copper medium for different energy ranges.

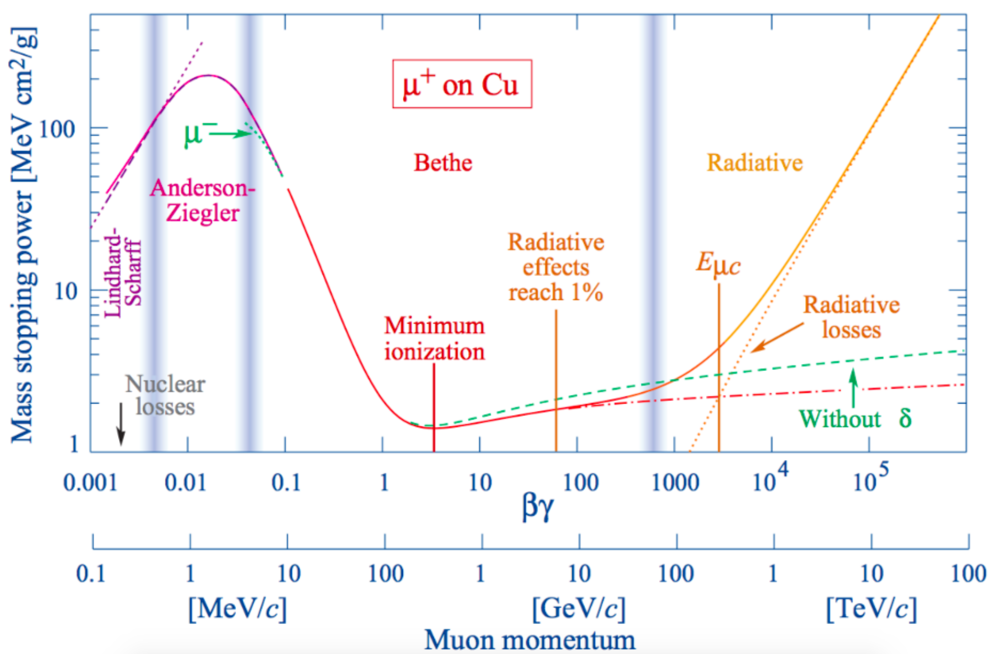

Figure 1.5: The plot shows the energy losses of muons passing through copper in various momentum ranges. For muons of greater than 10 GeV, photon bremsstrahlung (radiation) becomes significant and dominates for muons of more than a few hundred GeV. Picture from PDG.

But this is considering a single scattering. In a medium there will be multiple nucleons, so multiple scattering sites. A high energy particle undergoing multiple soft scatterings from a medium will experience interference effects between adjacent scattering sites. If the momentum transfer is small, the photon has small momentum and large wavelength and therefore it is not localized in space. A photon with definite energy (energy $\sim$ frequency $\sim$ 1/wavelength $\equiv 1/\lambda$) cannot be said to exist in a space interval much shorter than its wavelength, it takes some time for the photon to form. The time is of the order of λ/c for a particle traveling at velocity c. If the particle scatters from a second scattering center before the emitted photon is formed, it interrupts its formation process, reducing the per-center scattering probability. So as the longitudinal momentum transfer gets smaller the particles wavelength will increase and if the wavelength becomes longer than the mean free path in the medium (where the mean free path will be the average distance between scattering sites) then the scatterings can no longer be treated as independent events. This is the so-called LPM effect.

One of the possible outcomes is that even if a particle interacts with three different scattering centers it can emit only one photon. Thus the LPM effect can suppress bremsstrahlung photons.

1.5.2 QCD Bremsstrahlung

In QCD, just like in QED, coherent suppression of the radiation spectrum takes place when a quark (or a parton, for that matter) propagates in a medium. When a high-energy parton travels a length L of hot or cold matter, the induced radiative energy loss is proportional to L^2 when below the critical length [8].

But how can there be quark energy loss when quarks are confined? When a quark is knocked-out from a hadron it only enters a hadronization state after a macroscopically large time interval from the start of the process that is proportional to the quark energy much like the previous picture of the emission of a photon that takes some time to form. In the present case we call it the field regeneration time.

Field Regeneration Time

In a DIS hard process a quark is knocked out from a hadron as a half-dressed particle, this means that the charge appears to have a truncated proper field (either electro or chromomagnetic) when also being accelerated. The regeneration of a stationary field surrounding a charge has been well understood in QED [9]. The regeneration time of the proper field is given by:

$$T_{regen.}(k) \sim \frac{k_{\parallel}}{k_{\perp}^2} \tag{1.9}$$

where longitudinal and transverse components of photon momentum are defined with respect to the outgoing electron.

We can look at this problem from a classical point of view: considering a classical charge moving along the $z-$axis with velocity $v \approx 1$ after being accelerated from a $v = 0$ state at $t = 0$. At some point it will be surrounded by a Lorentz contracted electromagnetic field but it could not have emerged instantaneously. In the reference frame accompanying the charge the field spreads out inside the sphere $r' \leq t'$ but in the laboratory frame time it is slowed by $\gamma = E/m$, so the field changes will appear at distance r no sooner than at

$$t = \gamma t' = \frac{E}{m} r \tag{1.10}$$

The consequence of this for a quark is that it will have some time before hadronizing to interact with other partons. In this case r in Equation 1.10 will be the typical value of interquark distances inside a hadron of hadronic size R and m is its constituent mass. If we are dealing with a light quark (q = u, d, s) r and m are linked to each other by:

$$m \sim \sqrt{\langle k_{\perp}^2 \rangle} \sim R^{-1} \approx \text{a few hundred MeV} \tag{1.11}$$

So for light (q) and heavy (Q = c, b, t) quarks the estimation for the hadronization times are:

$$t_q^{hadr} \approx E R^2 \tag{1.12}$$

$$t_Q^{hadr} \approx \frac{E}{m_Q} R \tag{1.13}$$

Quark energy loss can be classified in two main classes: **collisional** energy loss and **radiative** energy loss.

1.5.3 Collisional Energy Loss

Collisional energy loss comes from an elastic scattering of the parton. In this case the scattering center recoils and carries away some energy. The energy loss per unit length is proportional to the strong coupling constant squared (α^2) temperature squared (T^2) and to a term with $\log(E/T)$ where E is the energy of the incoming parton that is losing energy as can be seen in 1.14. For heavy ion collisions the temperature is high, but for cold nuclei it's close to zero. The energy loss for a plasma is then

$$-\frac{dE}{dz} = \pi\alpha^2 \sum_p C_p \int \frac{d^3k}{k} \rho_p(k) \ln \frac{q_{max}^2}{q_{min}^2} \simeq \frac{4\pi\alpha_S^2 T^2}{3} \left(1 + \frac{N_f}{6}\right) \ln \frac{cE}{\alpha_S T} \tag{1.14}$$

where ρ_p is the density of the plasma constituents p (with momentum k). Below is a plot from [8] of numerical values for the collisional energy loss for a charm quark in a hot plasma.

1.5.4 Radiative Energy Loss

Radiative energy loss is caused by radiation of gluons, is what we previously called "gluon bremsstrahlung" in analogy with the QED radiation of photons.

Consider a very energetic quark of energy E propagating through a QCD medium of finite length L. Multiple scattering of this projectile in the medium induces gluon radiation, which gives rise to the radiative quark energy loss. To simplify the calculations, the scattering centers are assumed to be static and uncorrelated. For static (fixed) scattering centers, collisional energy loss is zero by definition.

One can define a parton-particle cross section $d\sigma/dQ^2$ where Q^2 is the momentum

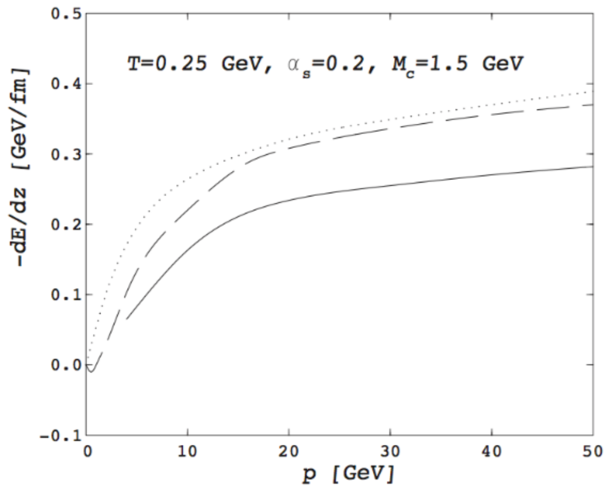

Figure 1.6: The plot shows the collisional energy loss of a charm quark as a function of its momentum. The dashed curve shows the equilibrium result; the dotted curve shows an original prediction by Bjorken. Taken from [8].

transfer. In the case of a hot QCD plasma, the "particle" is a quark or gluon, and in the case of cold matter (the case for this work), it is a nucleon. There is a momentum scale μ that is a characteristic of the medium: taken as the Debye screening mass in the hot case and as a typical momentum transfer in a quark-nucleon collision. The condition that the independent scattering picture is valid may be expressed as $1/\mu \ll \lambda$, where $\lambda = 1/\rho\sigma$ is the parton mean free path in the medium of density ρ. We assume that a large number of scatterings take place, that is, $L \gg \lambda$. Following the calculations from [8] one can find the Equation 1.15 that shows that the energy loss is proportional to the pathlength in the medium.

$$-\frac{dE}{dz} \simeq \frac{\alpha_S}{\pi} N_c \frac{\mu^2}{\lambda} L \tag{1.15}$$

To get to this equation the multiple scattering process is modeled after a Gaussian-distributed random walk in transverse momentum. The model (conceptually) takes steps through the medium. Each step has a length in time equal to the mean free path. At each step the particle can acquire an additional amount of transverse momentum. The average squared transverse momentum is just equal to μ^2. The derivation of the following equations can be found in more detail in [8].

We can define three regimes. In the **Bethe-Heitler regime** (BH regime in analogy to the QED Bremsstrahlung formula) $l_{coh} \leq \lambda$ and $\omega \leq \omega_{BH} \equiv E_{LPM}$ and the radiation is incoherent, every scattering results in a fully formed gluon before the next scattering. The spectrum only depends on the density times the cross section because it is just the sum of the result of individual independent scatterings in the medium of thickness L:

$$\left.\frac{\omega d^2 I}{d\omega dz}\right|_{BH} = \frac{1}{L}\left.\frac{\omega dI}{d\omega}\right|_{L} \simeq \frac{\alpha_S}{\pi} N_c \frac{1}{\lambda}. \tag{1.16}$$

Since $\lambda = 1/\rho\sigma$ is the parton mean free path, there is more emission for dense systems than for diffuse systems (e.g. QGP vs. cold nuclei) and for bigger parton-particle cross sections σ. The energy loss is visibly linear in path length, as can be seen from Equation 1.16 by integrating over z and then over ω.

The **coherent regime** is the so-called LPM regime and is defined by $\lambda < l_{coh} < L$ ($N_{coh} > 1$) so:

$$E_{LPM} = \omega_{BH} < \omega < min\{\omega_{fact}, E\} \tag{1.17}$$

with $\omega \sim \frac{\mu^2}{\lambda} L^2$, and ω_{fact} is discussed below. This means that the emission of one gluon is stimulated by several scattering centers coherently. In this case the step size in distance dz can be approximated by the coherence length itself $dz \approx l_{coh}$ because the gluon emission cannot depend on smaller distance steps since the coherence length is the smallest distance interval that can physically matter. We consider N_{coh} groups of partons that act as effective single scattering centers so the energy spectrum is estimated as:

$$\left.\frac{\omega d^2 I}{d\omega dz}\right|_{LPM} \simeq \frac{1}{l_{coh}}\left.\frac{\omega dI}{d\omega}\right|_{l_{coh}} \simeq \frac{\alpha_S}{\pi} N_c \frac{1}{l_{coh}} \simeq \frac{\alpha_S}{\pi} N_c \sqrt{\frac{\mu^2}{\lambda}\frac{1}{\omega}}. \tag{1.18}$$

If the equations for the spectrum of incoherent and coherent scattering are compared (equations 1.16 and 1.18) it is easily observed a suppression factor of $\sqrt{E_{LPM}/\omega}$ which makes sense since the coherence length is longer than the mean free path, that means the spectrum should be suppressed indeed.

But we can also think of another picture: when all the scattering centers act as one. This is the **factorization regime** and is characterized by $\omega_{fact} < \omega < E$ and $l_{coh} \geq L$ so:

$$\omega > \omega_{fact} = E_{LPM} \left(\frac{L}{\lambda}\right)^2 \tag{1.19}$$

$$\left.\frac{\omega d^2 I}{d\omega dz}\right|_{fact} \simeq \frac{\alpha_S}{\pi} N_c \frac{1}{L} \tag{1.20}$$

This term does not depend so much on the medium, it does not explicitly depend on the mean free path, density, interaction cross section, etc. But it does depend on the path length L, which is not constant for a realistic system such as a spherical nucleus or a QGP.

So from equations 1.16, 1.18 and 1.20 we can define a critical length L_{cr} where these expressions hold for a medium of finite length L if $L < L_{cr}$ and if $E > E_{cr} = E_{LPM}(L/\lambda)^2$, where:

$$L_{cr} = \lambda \sqrt{E/E_{LPM}} \tag{1.21}$$

So the energy loss expression in 1.14 is obtained when the gluon spectrum is integrated over ω, with $0 < \omega < E$. If the expression is integrated over z the total loss grows with L^2. For $L > L_{cr}$ equation 1.14 becomes:

$$-\frac{dE}{dz} \simeq \frac{\alpha_S}{\pi} N_c \sqrt{\frac{\mu^2}{\lambda} E} = \frac{\alpha_S}{\pi} \frac{N_c}{\lambda} \sqrt{E_{LPM} E} \tag{1.22}$$

so the size does not affect the energy loss per unit length and it is proportional to $\sqrt{E}$.

To obtain a general energy loss expression for the induced and the factorization cases as a function of L like in Fig. 1.7 and of the form:

$$-\Delta E \equiv \int_0^L -\frac{dE}{dz} dz \tag{1.23}$$

In [8] the authors use the random walk expression for the accumulated transverse momentum of the gluon due to successive scatterings in a medium of size L and they find:

$$\langle k_\perp^2 \rangle_L \simeq \mu^2 L/\lambda \tag{1.24}$$

and putting it into 1.14:

$$-\frac{dE}{dz} \simeq \frac{\alpha_S}{\pi} N_c \langle k_\perp^2 \rangle_L \tag{1.25}$$

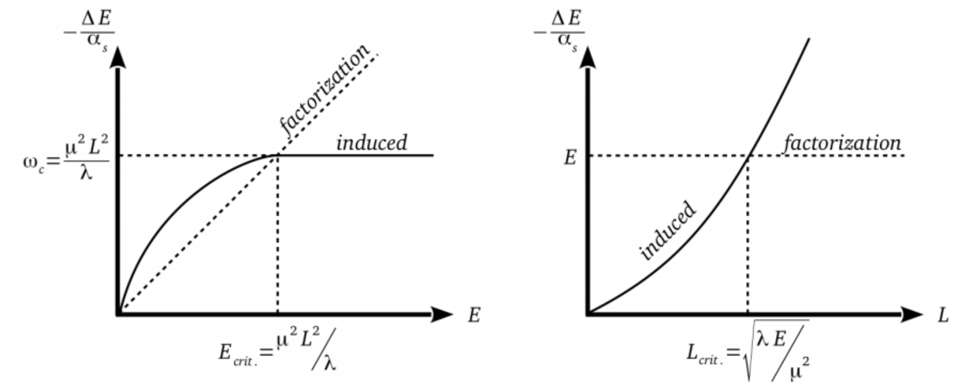

Figure 1.7: Schematical representation of total induced energy loss as a function of the parton energy E (left) and total induced energy loss as a function of the medium size L (right). From O. Aravena's thesis [10]

Figure 1.7 shows the energy loss as a function of the parton energy and as a function of the medium size. In the present case we will measure the direct energy loss for three different size media, the three EG2 targets, and binned the data in ν, expecting to observe this behaviour.

Chapter 2

Experimental Setup

The data used in this work is from the EG2 experiments, carried out from January 9, 2004 to March 5, 2004, in Hall-B at Thomas Jefferson National Accelerator Facility (Jefferson Lab), in Newport News, VA, USA. The Jefferson Lab is one of seventeen Unites States national research facilities overseen by the Office of Science of the United States Department of Energy (DOE) and is specialized in studying the structure of nuclear matter with its particle accelerator, the Continuous Electron Beam Accelerator Facility (CEBAF) based on superconducting radiofrequency (SRF) technology, and the different detectors from Halls A, B, C and D.

In this work the data used is from Hall B, and its main detector is called CLAS (CEBAF Large Acceptance Spectrometer) [11]. CLAS was designed to operate with electron beams of 5.014 GeV with a momentum resolution of 0.01$\%$ and a typical diameter of 50-100 μm during the EG2 run period, produced by CEBAF. A schematic of the facility, including the accelerator and the experimental halls, can be seen in Fig. 2.1 and the next sections go into more detail about the specific parts of the experiment.

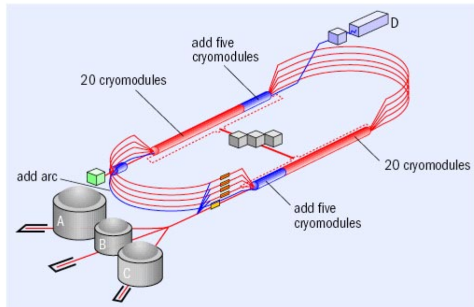

Figure 2.1: CEBAF accelerator and experimental halls. This is the 12 GeV upgrade.

2.1 CLAS

Hall B hosts the CEBAF Large Acceptance Spectrometer (CLAS), one of the detectors that receives electron beams produced by the CEBAF accelerator and has a wide solid angle range of almost 4π, while the Halls A and C focus on high resolution and Hall D started only in 2014 and after the experiment used for this analysis.

One of the most particular features of the CLAS detector is its toroidal magnetic field. It is generated by six superconducting coils placed around the beam axis and was designed this way for better measurement of charged particles, producing better momentum resolution while maintaining the area close to the target unaffected by the magnetic field, making possible to perform experiments with polarized targets.

The detection system is a collection of different elements used for different purposes. The Drift Chambers (DC) are used to determine the trajectories made by charged particles, Cherenkov Counters (CC) are for electron identification and pion rejection, Scintillator Counters (SC) are used for measuring Time-of-Flight and Electromagnetic Calorimeters that measure energy deposition by charged particles as well as neutral particles, detecting electrons and photons and helping in the detection of neutrons (when combining information from the different elements of the detector).

The location of the six coils that generate the toroidal field, naturally separates CLAS in six sections. A small mini-torus surrounds the target so that in electron scattering experiments low momentum electrons produced by Møller scattering are kept from reaching the drift chambers. Fig. 2.2 shows a schematic view of the detector and

Fig. 2.3 is a perpendicular view.

Because of the way the detectors are organized it is best to describe the geometry of the experiment with spherical coordinates. The z-axis lies along the beam direction, θ is the polar (scattering) angle and ϕ is taken as the azimuthal angle while x is the horizontal and y the vertical directions in the plane that is normal to the beam.

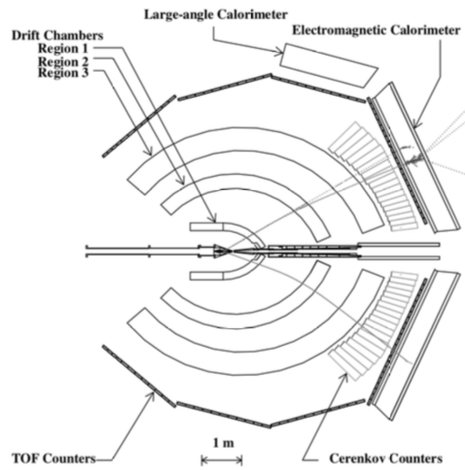

Figure 2.2: CLAS viewed along the beam line with an illustration of a typical photon, electron and proton tracks from an interaction.

2.1.1 Torus Magnet

For the measurement of momentum of charged particles, the magnetic field generated by the six iron-free superconducting coils that produce a toroidal field around the beam axis is used. It can be calculated directly from the current since there is no iron in the system. These are used for charged particles since the field bends the particles' trajectories towards or away from the beam axis (depending on the sign of the charge) and leaves the azimuthal angle essentially unchanged, while the neutral particles trajectories remain unchanged. The magnet coils are approximately 5 m in diameter and 5 m in length. Fig. 2.4 illustrates the coils and fields of the system. While the main component of the field is in the ϕ-direction, close to the coils there are significant deviations, but they are minimized by the circular inner shape of the coils so the particles that come

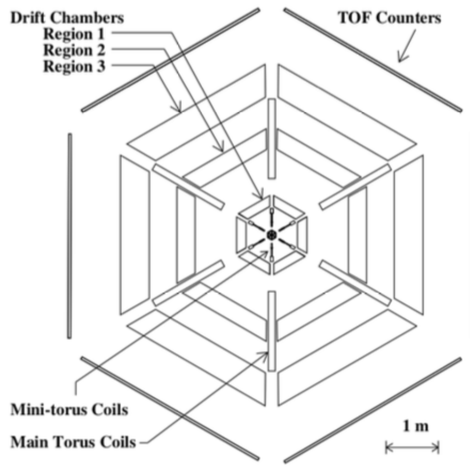

Figure 2.3: CLAS schematic perpendicular to the beam direction. The location of the Drift Chambers, Torus Magnets and TOF Counters are indicated.

from the target do not experience a significant deflection in ϕ when crossing the inner boundary of the coil.

2.1.2 Drift Chambers (DC)

The drift chambers are actually 18 separate chambers in each of the six sectors (separated by the magnet coils) which in turn are grouped in three chamber regions located radially from the beam that share many of the same basic design elements. They are wedge-shaped constructed from a pair of long wire-supporting endplates that bear both the load of the wire tensions and the weight of all associated hardware.

Each region experiences the magnetic field at different intensities. The closer ones to the targets are the Region One chambers and they are localized in a low field intensity area. The Region Two chambers are placed between the magnet coils where the intensity of the magnetic field is the highest. And the Region Three chambers are outside the magnetic coils.

To accommodate the wires, there are two endplates parallel to the closest coil planes (60^o with respect each other) with the wires stretched between them. These wire layers are grouped into two bigger layers of six layers each. One is axial to the magnetic field

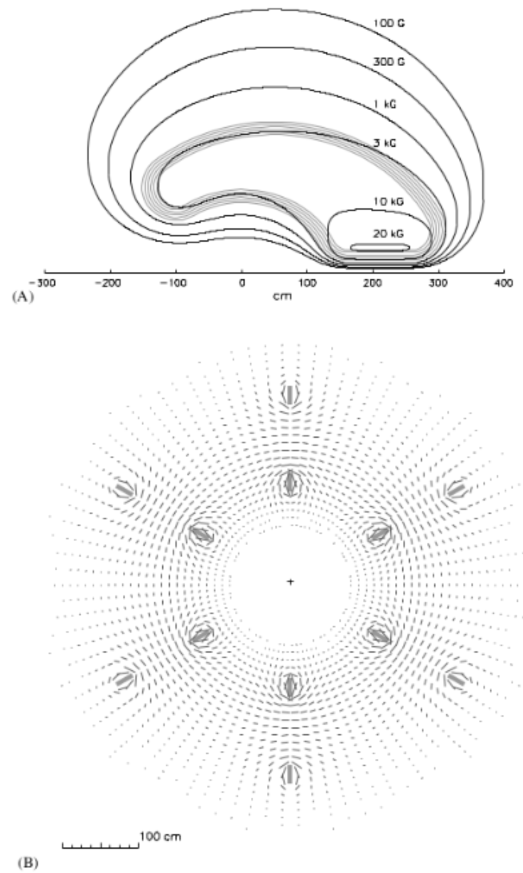

Figure 2.4: Magnetic field contour produced by the super conducting coils.

while the other is tilted by a 6^o stereo angle to provide azimuthal information. Only Region One is different, with only four wire layers in the first super layer since it has less space available. So it has only 4 layers in the innermost super layer and 6 in the next to that. The wire layout can be seen in Fig. 2.5.

More details on the drift chamber system can be found in [12].

2.1.3 Cherenkov counters, CC

The main goal of the Cherenkov Counters is to trigger electrons while also discriminating them from pions. In each of the six sectors the CCs cover up to $\theta = 45^o$ and

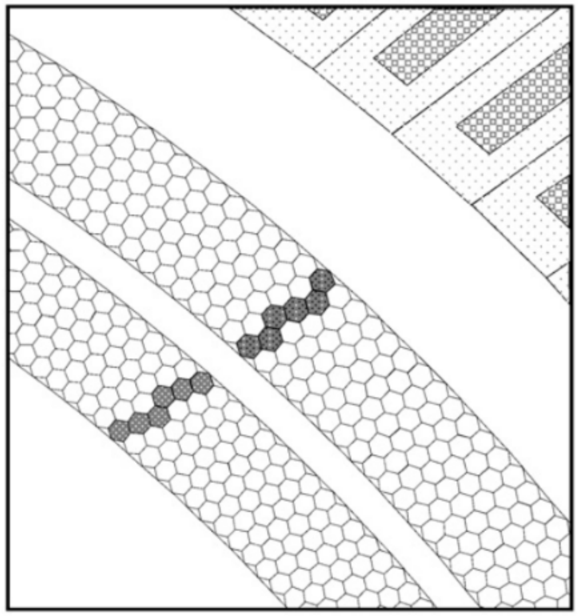

Figure 2.5: The Region Three chamber. A layout of its two superlayers and its wiring. The sense wires are at the center of each hexagon and the field wires are located are the vertices. An example of a passing particle track is shown by the highlighted drift cells that have fired (from [13]).

are constituted by mirrors, that cover most of the available area, PMTs, placed in a ϕ region that is covered by the magnetic coils so they don't intercept the particle's trajectories, and a radiator gas, that causes the Cherenkov radiation. A schematic of the detector can be seen in Fig. 2.6. The goal of its design is to have a small amount of material in the sensitive area to prevent degradation of energy resolution. The mirrors are organized in a specific way so they reflect the Cherenkov light produced from the particles to the location of the PMTs, which in turn collect the light and convert it to an electronic signal that can be analysed. Since the charged particle trajectories lie in planes of constant ϕ, the placement of the PMTs does not affect the angular coverage. And the mirrors focus the light only in the ϕ direction, preserving the information of the polar angle θ of the electron. Also, since the PMTs are located in the region with highest transverse magnetic fields, they are covered with high permeability magnetic shields.

To cause the emission of light from the particles a radiator gas is used. In this case perfluorobutane (C_4F_{10}) was used with a refractive index of 1.00153, resulting in a pion momentum threshold of 2.5 GeV/c. An inbending electron, for example, passing through the active volume of the detector results in typically 4-5 photoelectrons that will be reflected to the PMT's and then amplified by the last.

More details on the CLAS Cherenkov detector can be found in [14].

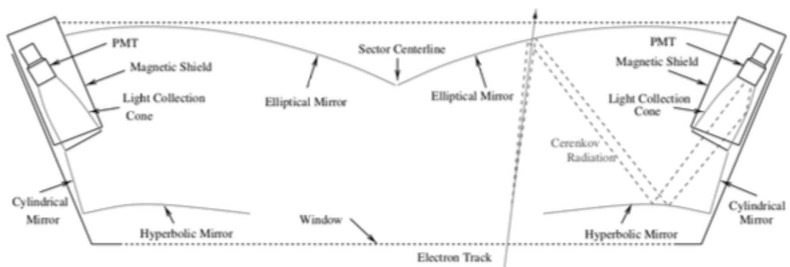

Figure 2.6: Diagram of a Cherenkov Counter segment, symmetric around the sector center. An example of an electron trajectory with the collection of Cherenkov light to the PMT is shown. The PMTs, magnetic shields, and light-collecting Winston cones lie in the region of the detector covered by the CLAS magnet coils, so it does not affect the electron acceptance.

2.1.4 Time-of-Flight Counters (SC)

These detectors are located between the CC and the calorimeters (as seen in Fig. 2.2 and Fig. 2.3), covering a polar angles of $\theta = 8^o$ and $\theta = 142^o$ but the entirety of the active range of ϕ. They are made of 5.08 cm thick scintillators positioned perpendicularly to the average local particle trajectory. At forward angles $\theta < 45^o$ the counters are 15 cm wide and 32 - 376 cm in length, and at large angles the counters are 22 cm wide and 371 - 445 cm in length resulting in 206 m^2 of scintillators.

More details on the Time-of-flight system can be found in [15].

2.1.5 Forward Electromagnetic Calorimeters (EC)

This detector is used mainly for electron detection of energies above 0.5 GeV, photons of more than 0.2 GeV, and neutrons. They are made of layers of scintillator strips alternated by lead sheets, totaling a thickness of 16 radiation lengths. Each lead sheet has a thickness of 0.24 of that of the scintillator so they have a total of 8.4 cm and 39 cm of each respectively. It uses a projective geometry in which the area of each successive layer increases.

Each EC module has 39 layers, made with 10 mm individual scintillators and 2.2 mm individual lead sheets making a triangular volume. The scintillator layers consist of 36 parallel strips which are rotated 120° after each layer, thus defining three views (U, V and W), which provide stereo information on the location of the energy deposits. Each one of the views has 13 layers each as seen in Fig. 2.7 and are further subdivided into an inner (5) and outer (8) stack, providing longitudinal sampling that helps to improve hadron/electron separation.

For the detection of neutrons the EC were provided with its own timing system, independent of the TOFs. It is used to differentiate photons and neutrons, and is sufficient to provide a start time in case any channels in the TOFs are inoperative in the forward region. So with that, neutrons can be detected by a combination of information from the electromagnetic calorimeter, drift chambers and time-of-flight.

More details on the CLAS forward electromagnetic calorimeter system can be found in [16].

2.2 Double-Target System

The target system was designed specifically for the EG2 Experiment. The goal of the experiment was the precision measurement of nuclear medium effects, like hadron attenuation and transverse momentum broadening, and also to search for color transparency in unpolarized electron scattering through the attenuation of rho meson in nuclei with an electron beam of 4-5 GeV.

To minimize the systematic uncertainties the target was designed to be a double-

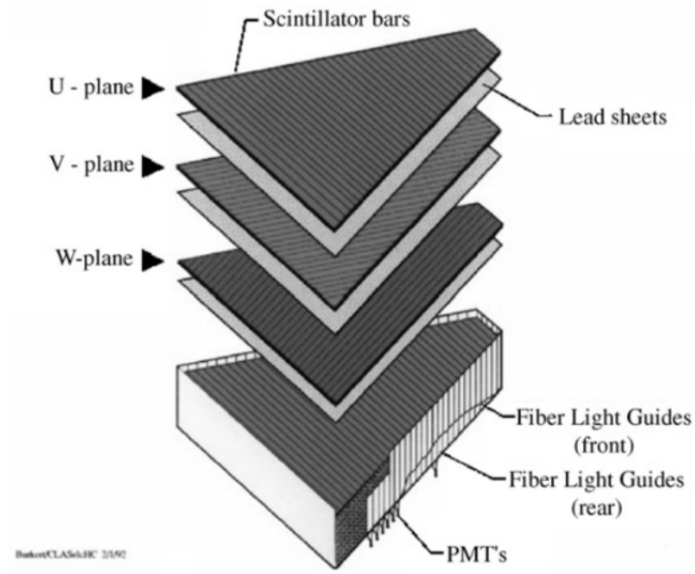

Figure 2.7: Exploded view of one of the six CLAS electromagnetic calorimeter modules.

target, where a solid (carbon, aluminim, tin, iron or lead) and a liquid (deuterium) target were simultaneously located in the beam line and separated by 4 cm so the acceptance correction differences are minimized while the ability to identify the target event by event is maintained. This also results in same beam current reducing the errors in the estimation of the ratio of the cross-sections.

To achieve the goal of the EG2 Experiment, the target also had to have some key features: a large acceptance for semi-inclusive and exclusive kinematics, a good match to the CLAS detector acceptance, minimal mass for low-energy particles at large angles (70°-140° from the beam direction) as well as forward particles, similar scattering rates for the two targets in the beam, minimal mass in the support structure, rapid target changes for the heavy nuclear targets, less than 2-3% of a radiation length of any target material to suppress secondary electromagnetic processes, and minimal entrance/exit window thicknesses for cryotarget to maximize target/window ratio. One of the targets needed to be a stable deuterium cryotarget, while the second was a solid, heavy nuclear target. The cryotarget was located upstream of the solid targets, limiting the effects of secondary electromagnetic processes contributing to the flux incident on either target.

A schematic of the cryotarget can be seen in Fig. 2.8. A full assembly of the double target is shown on Fig. 2.9. Each holder arm carries a different target and can be flipped on and off remotely to change the target on beam.

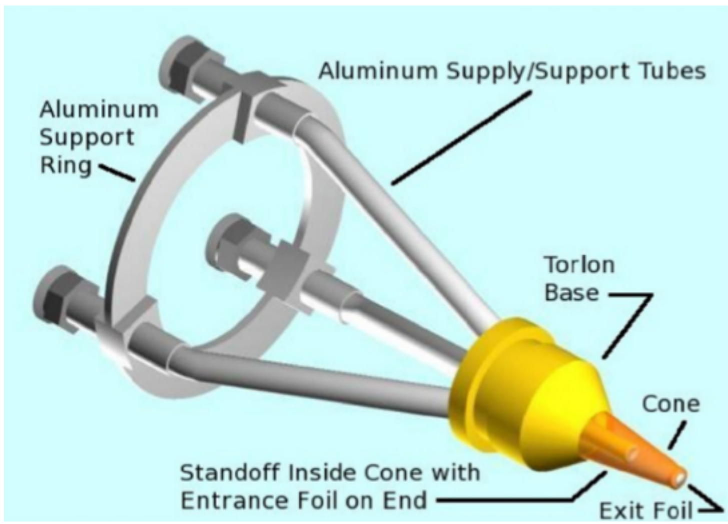

Figure 2.8: A drawing of the cryotarget cell showing the three support tubes through which the cryogens flow; the entrance foil attached to the cylindrical standoff; and the exit foil attached to the outer cone. The electron beam passes through the center of the support ring in the upper left part of the drawing, then through the entrance and exit foils in the lower right part of the drawing.

More details on the target system can be found in [17]. A GEANT3 simulation of the double target system was added to the existing simulations of the full CLAS detector.

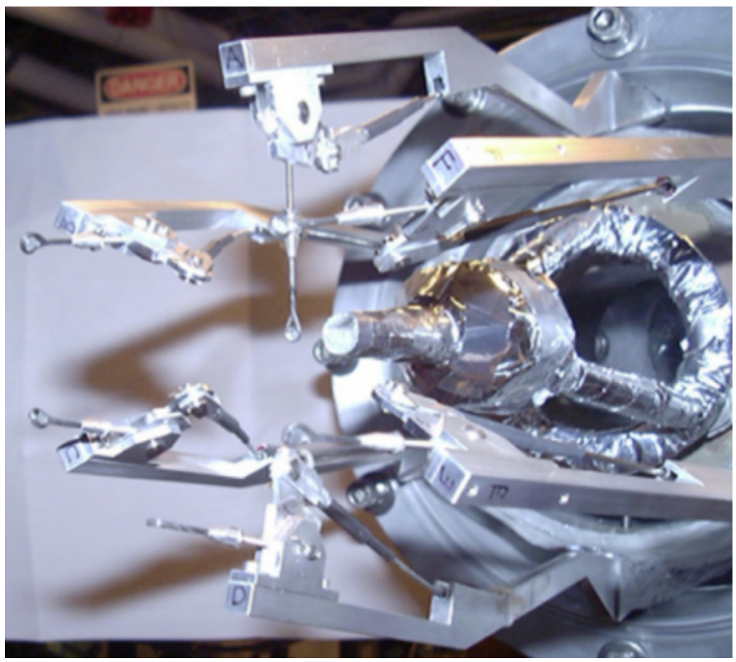

Figure 2.9: The full double-target assembly, which shows one solid target flipped into position; five solid targets retracted; and the thermally insulated cryotarget cell (from [13]).

Chapter 3

Data Analysis

3.1 Data Format

The raw data taken from the experiment was stored in files for each run in Bank Object System (BOS) format. For each file the data were organized in units of information corresponding to certain detectors called banks. The reconstruction procedure for the conversion of raw data into particle information useful for an analysis is named "cooking". This was performed using USERANA software, which gives information of the reconstructed tracks also in BOS format. All cooked data were organized in events, by event we mean that the scattered electron passed the triggering threshold and all the reconstructed particles detected after the trigger are also included. After cooking the data with USERANA the files have to be converted to ROOT [18] format. This step was performed using the ClasTool software. It was created by Maurick Holtrop and Gagik Gavalyan and it is a ROOT based package for analysing CLAS data. It organizes the information in a structure using NTuple objects from ROOT, where the links between different banks are included as pointers.

The last step is to use Analyser [19], a C++ based class, that takes the data from ClasTool and reduces it to NTuples with general information of the particles. This process is important since it produces files in a simpler format for the analysis, making it a lot easier to work with.

3.2 Particle Identification

One of the parts of the data analysis is to attempt to identify each of the particles detected. For that we make a few different "cuts" in the data: cuts in the *data banks* allow us to select particles based on the detector used for the specific signal, cuts in the variables can be performed to reject some contamination of the sample, and the *fiducial cuts*, that exclude the regions of the detectors that have efficiency problems. Some of the cuts performed are described in the next sections.

3.2.1 Electron Identification

Since the particles in the EVNT bank are ordered according to the time they arrive at the SC, to identify the scattered electron we consider the first track in the bank. Not only that but to classify an event as a "good" event, the first particle identified must be an electron. Also, some particles leave tracks in all detectors and others only leave tracks in some of them. So first of all, the basic requirements to identify a particle as an "electron" are two: The particle must leave a track in all detectors (DC, CC, SC, EC); and the charge must be negative.

The electrical charge of the particles is extracted from the curvature of the tracks in the DC, since they go through the magnetic field produced by the torus magnet. If the particle bends inwards it has a negative electric charge, and if the particle is positive its track will bend outwards with the default tourus field direction.

If these requirements are fulfilled the next step is to make π^-/e^- separation by using the information in the CCPB branch (a bank related to the Cerenkov Counters). The e^- can be differentiated from the π^- by measuring the electromagnetic radiation emitted by them when passing through a medium. This radiation, called Cherenkov light, is the electromagnetic radiation emitted by a charged particle when passing through a medium with a velocity that is larger than the velocity of light in this medium. A minimum momentum threshold for each particle is required so it can emit Cherenkov radiation and it depends on the mass of the particle. In this case, charged pions need a minimum momentum of 2.5 GeV to emit Cherenkov light, compared to electrons that need just a few MeV. From the distribution of the number of photons collected by the PMTs of the CC, a clear peak with low number of photo-electrons is observed. This peak correspond to the π^- signal. So in order to select a particle as an electron a minimum number of 2.5 photo-electrons is required in each of the CC sectors.

Another cut in the EC bank is made with the same goal of suppressing pion contamination. The EC only covers forward angles and the scattered electron always travels in a forward direction while the pion can have any direction. So any track not producing a signal in EC is immediately rejected. To complement that, since pions are minimum ionizing, they will deposit a fixed amount of energy in the detector, regardless of its momentum.

In addition to the preliminary identification described above, some additional cuts and selections are necessary to assure the quality of the data. One of the consequences of having the detector separated in six sectors is that we will have regions with poor acceptance. For example, not all particles from an electromagnetic shower will be detected if the particle that generated it hit the edge of a detector, since the shower will not be fully contained by it. So to reduce systematic uncertainties it is necessary to select a fiducial volume where the acceptance is large and uniform, these are the so called "fiducial cuts". They remove the data near the edges of the detectors and were developed by Lorenzo Zana.

More details of these and all the cuts performed can be found in [20].

3.2.2 π^+ Identification

The procedure of identifying pions is analogous to the electron. So besides requiring a positive general status for the event the hit must be positively charged since the particle of interest on this analysis is the positive pion π^+. So the thing to do is to discriminate them from other positive hadrons and positrons. Positive pions were identified using positive reconstructed tracks with track signals in the SC, DC.

To select positive pions and exclude the kaon and proton contamination the "time-of-flight" (TOF) discrimination technique was used. The technique consists of using the information from the tracking system in conjunction with the TOF system, determining the time difference between a positive hit and an outgoing electron. This time difference is called TimeCorr4 (Δt) and is of the following form:

$$\Delta t = \frac{L^{e^-}_{flight}}{c} - t^{e^-}_{flight} + t_{flight} - T_{RFI} - \frac{L_{flight}}{\sqrt{\left(\frac{M_{\pi^+}}{p}\right)^2 + 1}} \tag{3.1}$$

where $t^{e^-}_{flight}$ and t_{flight} represent the time for flight from the interaction vertex to the scintillator of the electron and charged particle, respectively. $L^{e^-}_{flight}$ and L_{flight} are the path lengths from the vertex to the TOF counters. M_{π^+} and p are the π^+ mass and the momentum of the charged particle. The T_{RFI} is an additional timing correction using the radio frequency signal sent from the accelerator injector.

What was done here was the comparison of the theoretical time for a π^+ with a given momentum with the measured time taken for the particle to reach the SC detector. If we are looking for π^+ but the detected particle is lighter/heavier it would take less/more time to reach the SC than the time that was calculated. So cuts in data are made around 0[ns] of time difference between the calculated and the measured time. These cuts are for pions of P < 2.7 GeV.

Besides the TOF technique we need additional cuts for pions with P > 2.7 GeV. First a non null number of CC hits and a positive status in the CC data bank are required. After that some geometrical matching is also needed. We also make sure that the pion candidate must fail the positron cuts and the positron is defined in the same way as the electron, but this time the charge must be positive.

Pions with more than 2.5 GeV start emitting Cherenkov radiation so the Cherenkov Counters are used for pions with energies of that range. As mentioned before a requirement of at least 2.5 photo-electrons emitted is made.

The fiducial cuts were made similarly as the ones applied for the electron identification. A cut in θ_{lab} and ϕ_{lab} variables was made to remove hits close to edges of the detector where acceptance is worse, and reconstruction is less reliable.

All the pion identification techniques are described in more detail in [20].

3.3 Additional Cuts

3.3.1 DIS Kinematics

Now that we have all good electrons and pions identified the next step is to select events with kinematics that corresponds to the DIS regime:

- According to the wave length of the virtual photon: $\lambda \approx 1/Q$, the selection of $Q^2 > 1.0$ gives enough resolution as to see the partons inside the nucleons.
- We are also not interested in hadrons coming from nuclear resonance decay (e.g. Δ^{++}) so to exclude those and avoid the resonance region a cut on the invariant mass of the electron-nucleon interaction of $W > 2.0$ is applied, where W is the invariant mass of the photon-nucleon system.
- Another possible source of the data contamination is the radiative effects. They become important for larger values of the DIS variable y, so a cut is made in $y < 0.85$.

3.3.2 Vertex Cuts

After selecting the electrons, pions and the DIS events it is necessary to identify the target at which the event occurred, the solid or the liquid target. Since both targets are located along the z-axis (which corresponds to the beam axis) a vertex cut is applied on the Z variable that represents the position of the vertex along the beam axis.

3.3.3 Feynman X

To reduce possible target fragmentation contribution we put a constraint on the Feynman X variable, x_F. For this work the requirement is of $x_F > 0.1$ to emphasize the current fragmentation region. When performing a x_F cut we observe a change in the shape of the energy spectrum and drop in statistics, which can be observed in Figure 3.1. The main goal by reducing fragmentation contribution is to ensure that we are using only hadrons from the struck quark.

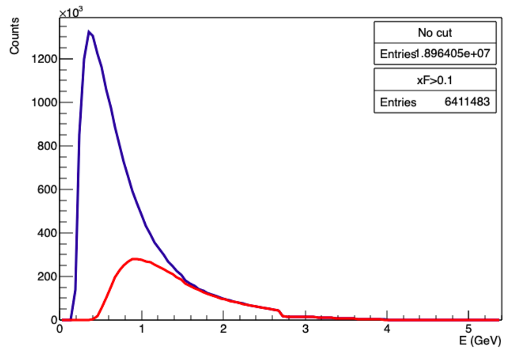

Figure 3.1: In this plot the red curve represents the energy spectrum with no Feynman X cut and the blue curve is the energy spectrum with Feynman X greater than 0.1.

Modified Feynman X

Something particular about this analysis is that the Feynman X cut for the shifted distributions had to be done a bit differently. This cut changes the shape of the energy distribution and x_F is defined as:

$$x_F = (\nu + m_p)\frac{\sqrt{p^2 - p_T^2} - (Q^2 + \nu^2)Z_h\nu/(\nu + m_n)}{\frac{1}{2}\sqrt{(W^2 - m_n^2 + m_{\pi^+}^2)^2 - 4W^2 m_{\pi^+}^2}} \tag{3.2}$$

In the method used to extract the direct quark energy loss we manually shift the energy spectrum of one of the targets towards the other one. That means we are changing the E value. From Equation 3.2 we can see that when the energy, x_F is also affected. That means that for each shift we need to recalculate the x_F in order to perform the right cut. The Feynman X of the shifted spectrum is what we will call modified Feyman X x_F^{mod} and it can be defined as:

$$x_F = (\nu + m_p)\frac{\sqrt{(p + \Delta E)^2 - (1 + \Delta E/p)^2 p_T^2} - (Q^2 + \nu^2)(Z_h\nu + \Delta E)/(\nu + m_n)}{\frac{1}{2}\sqrt{(W^2 - m_n^2 + m_{\pi^+}^2)^2 - 4W^2 m_{\pi^+}^2}} \tag{3.3}$$

3.4 Simulations

Ideally, the result of any experiment should be detector independent but the CLAS detector has some unavoidable difficulties which end up reducing the data obtained from the experiment. For one, CLAS's geometry does not cover the full momentum space range of the phenomena studied in the experiment, but not only that the detectors and the reconstruction protocol also have limited efficiency. Because of that we should correct the results for the acceptance effects.

To correct for acceptance we need to know what should the data set look like *before* going through the detectors as well as how this data behaves when interacting with the detector. All that is done by means of simulations.

The simulations used in this work were produced by Hayk Hakobian and are explained in detail in [13]. They consist of two sets of events, the generated and reconstructed events.

The generated events were produced with Pythia 6.319, a Monte-Carlo event generator. It contains a model of non-perturbative and perturbative DIS processes. The simulation set consists of approximately 100 million events for each target. The output of the Pythia simulation are the generated events, or what we call "thrown", and those are fed to the GSIM.

GSIM creates a model of the CLAS spectrometer and simulates how the detector would respond to MC generated events. It is built with GEANT 3 simulation package (CERN software) as the base and the features of the EG2 target were implemented by Hayk Hakobyan [13]. They include processes like energy loss and radiation of secondary particles through different parts of CLAS.

After that the GSIM Post Processor (GPP) was used in order to account for defects that the detector might have and to eliminate signals from dead channels, like dead wires in the drift chambers and bad tubes in the scintillator counters.

Then the GPP output files go through a reconstruction process, using the RECSIS program, just like the real data. The reconstruction program was built with the same libraries that were used for the processing of the real data from the EG2 running period. In the final stage, mostly the same cuts used on the experimental data were used on the simulated output data, we only had to account for a few differences between real data and simulations.

One of the differences is that the CC efficiency is much worse for data and some of the inefficient zones could not be simulated by the MC technique. The result of that is that the spectrum for the Number of Photo-electrons in the simulated data does not have a big peak, so some specific cuts were made to make it look like the real data. The cuts based on EC energy were also slightly modified. More details about these differences can be seen in [20].

3.5 Corrections

3.5.1 Acceptance Correction

This correction is based on a simulation factor applied to each bin in the experimental data with the goal of correcting the inefficiencies of the detector. In the case of the CLAS detector the acceptance is a combination of geometrical acceptance and inefficiencies in the drift chambers, scintillator counters, track reconstruction and event selection.

The acceptance correction factor A is calculated with the simulations described in Section 3.4 and are defined as:

$$A = \frac{N_{rec}}{N_{gen}} \tag{3.4}$$

where N_{rec} and N_{gen} are the number of counts in the bin for reconstructed and generated events, respectively. Since this correction is applied in each bin independently the binning used to calculate the factors must be the same used for the analysis of the real experimental data. Ultimately the data is corrected by a weight of $w = 1/A$.

Since the Kolmogorov test is very sensitive to fluctuations, in this work the acceptance correction was performed with the fitted distributions of acceptance factors. The calculations of the energy distributions acceptance factors were made bin by bin, matching the same number of bins that were later used for the statistical tests. After that the distribution was fitted and the fit function was used to calculate the correction factor. The process for this specific analysis is explained in more detail in Section 4.

3.5.2 Coulomb Corrections

For DIS experiments it is also necessary a Coulomb correction based on the effects that the Coulomb field of the target nuclei has on any particle that approaches it. This is especially important in our present case of low energies ($\sim$ 5GeV) and medium to heavy nuclei.

The incoming electron's momentum is enhanced as it gets closer to the nuclei and the momentum of the scattered electron gets reduced as it leaves the nuclei's vicinity. The Coulomb field also affects the π^+, the particle of interest in this thesis.

For the purpose of this thesis we will use the following ΔE Coulomb corrections from [21] shown in Table 3.1.

Target	ΔE [MeV]
^{2}D	0
^{12}C	2.9
^{56}Fe	9.4
^{208}Pb	20.3

Table 3.1: Coulomb correction ΔE values from [21].

3.6 Shape Analysis

This work is based on the shape analysis of the energy spectrum of pions from solid and liquid targets. The goal is to extract the quark energy loss ΔE that happens when a quark is crossing a nuclear medium. To do that we use events from the deuterium target as a control. Scatterings from the deuterium target are considered events where the quark was emitted in a "vacuum". The energy spectrum from those events is compared to the one of a solid target (C, Fe, Pb). Assuming that there is some energy loss when the quark travels through a nuclear medium (as discussed in 1.5) this solid target energy spectrum will be shifted horizontally in relation with the liquid target spectrum. This horizontal shift in energy will be identified as the quark energy loss.

The question is how to find this shift in energy. The proposed method is to make incremental shifts in the energy distribution of the solid target pions by summing δE to the measured energy. The resulting energy spectrum is referred to as "shifted distribution". Then we use a statistical test to compare the shifted distribution to the unchanged energy distribution of pions from deuterium target. This statistical test will give us the probability that both curves come from the same distribution. This process is repeated for a number of times N. After comparing all the horizontally shifted distributions we select the one that yields the highest probability for the test. This means that the selected distribution was produced by the correct ΔE and behaved like it would have if the pion were in a vacuum, and as if there were no energy loss happening. The statistical test chosen for this task was the 2-Sample Kolmogorov-Smirnov Test.

3.6.1 The Kolmogorov-Smirnov Test

The Kolmogorov-Smirnov test (KS test) is a statistical test that can be used to compare one dimensional distributions: a sample with a reference distribution, or two samples. The way it does that is by quantifying the distance between the the empirical distribution function of the sample and the cumulative distribution function of the reference distribution, in the case of the one sample test, or between the two empirical distribution functions if using two samples.

The null hypothesis is that the sample is drawn from the reference distribution or, in the case of two samples, that both come from the same distribution, and with that the null distribution is calculated. In the present work the two sample KS test was used, always comparing the energy distribution of the pions from the deuterium target with the pion's energy distribution from a solid target.

One of the reasons for using the KS-test is that it is a good general nonparametric method for comparing two samples and it is sensitive to location and shape differences between two cumulative distribution functions. Another attractive feature is that the distribution of the KS statistic does not depend on the underlying cumulative distribution being tested. It is also is an exact test, so it does not depend on the sample size for the approximations to be valid (like the chi-square test does). But we also need to keep in mind its downsides. The test works best with continuous distributions, it is also more sensitive near the center of the distributions than at the tails, and the distribution must be fully specified.

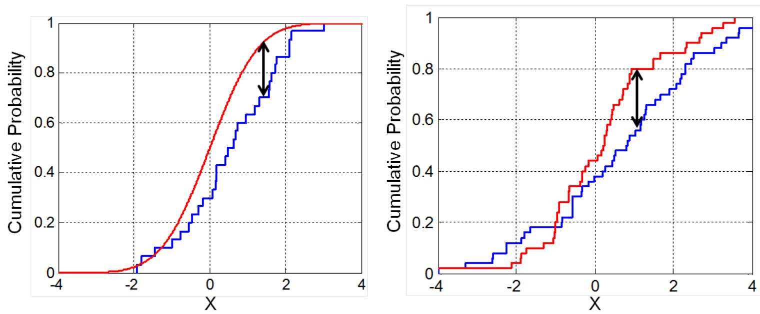

Figure 3.2: The Kolmogorov statistic. On the left a one sample example where the red curve is the model and the blue line is the sample. On the right an example of a two sample statistic.

3.6.2 Two-Sample Kolmogorov-Smirnov Test

The Empirical Cumulative Distribution Function (ECDF) F_n for n independent **ordered** observations X_i is defined as:

$$F_n(t) = \frac{\text{number of elements in the sample } \leqslant t}{n} = \frac{1}{n}\sum_{i-1}^{n} 1_{X_i<t_i} \tag{3.5}$$

and with that we can define the **Kolmogorov statistic**:

$$D_{n,m} = \sup_x |F_{1,n}(x) - F_{2,m}(x)| \tag{3.6}$$

where $\sup$ is the supremum function.

If the sample is large the null hypothesis is rejected at level α if:

$$D_{n,m} > c(\alpha)\sqrt{\frac{n+m}{n \cdot m}} \tag{3.7}$$

where in general $c(\alpha) = \sqrt{-\ln(\alpha/2) \cdot \frac{1}{2}}$.

The Kolmogorov Distribution

The Kolmogorov Distribution gives the probability that Kolmogorov's test statistic will accept the null hypothesis and can be defined as:

$$P(z) = 2 \sum_{j=1}^{\infty} (-1)^{j-1} \exp^{-2j^2 z^2} \tag{3.8}$$

where $z = \sqrt{\frac{m \cdot n}{m+n}} D_{n,m}$. The z quantity looks like the $c(\alpha)$ quantity from equation 3.7, so the Kolmogorov distribution gives the probability that Kolmogorov's test statistic will exceed the value z, assuming the null hypothesis.

3.6.3 The ROOT implementation

For this work a ROOT implementation of the Kolmogorov test and the Kolmogorov Distribution was used. There are two versions of this test in ROOT, a TH1F version and a TMath version.

TMath::KolmogorovTest

TMath's Kolmogorov Test uses two one dimensional **ordered** arrays as input and returns the calculated confidence level which gives a statistical test for compatibility of the two arrays.

The function calculates the maximum deviation between the two integrated distribution functions multiplied by the normalizing factor. The algorithm is a for-loop over the two arrays (a and b, e.g.) and handles the three different possible cases: $a > b$, $a < b$, $a = b$. The code basically keeps a tally with increments of one over the number of observations.

After calculating the maximum distance between the two distributions it calls a different function to calculate the probability, the TMath::KolmogorovProb

TMath::KolmogorovProb

This function does exactly what is described in Section 3.6.2 as the Kolmogorov distribution, with z as the input. So the output will be the confidence level for the null hypothesis.

TH1F::KolmogorovTest

This is a binned version of the Kolmogorov Test, so it uses histograms instead of arrays. The inputs are the histograms for both functions and the output is also the probability that both histograms have the same parent distribution.

Is is important to note that the Kolmogorov-Smirnov Test should in theory be only used for unbinned data and not for binned data, as is the case with histograms. For that we can use the TMath::KolmogorovTest. But if the data set is too large arrays are not the most efficient objects to work with, in this case histograms are extremely convenient. In principle, as long as the bin width is small compared with any significant physical effect (for example the experimental resolution) then the binning cannot have an important effect for the test. Therefore one can argue that for all practical purposes, the probability value given by the TH1F test is calculated correctly provided the user is aware that:

- The value of the probability given should not be expected to have exactly the correct distribution for binned data.
- The user is responsible for seeing to it that the bin widths are small compared with any physical phenomena of interest.
- The effect of binning (if any) is always to make the value of the probability slightly bigger than in the unbinned case. Setting an acceptance criteria of $p>0.05$ will assure that at most 5% of truly compatible histograms are rejected.

With all that in mind we designed a Proof of Concept with the goal of testing our method and comparing the different implementations of the Kolmogorov Test.

3.6.4 Proof of Concept

For our Proof of Concept we generate two random distributions, one of them with a small artificial shift, to represent the two spectra that we want to compare for the energy loss measurement. These distributions then go through all the same tests and algorithms that will later be used for real data. If we can extract the applied shift it means that our method works and that we can proceed and use it with real data.

So for each run of the Proof of Concept, or "experiment", consists of the following steps:

1. Generate two random distributions where one is shifted to the left by ΔE. For all Proof of Concept the artificial shift chosen was of 21.

2. Use the KS test to compare the two curves. This gives us a probability that both curves are equivalent.

3. Manually add δE, referred to as step, to each entry of the shifted distribution and repeat step 2.

4. Repeat steps 2 and 3 enough times to obtain a reasonable probability distribution.

5. Pick the $\delta E * N = \Delta E$ value that yields the highest probability value as the "found shift".

Gaussian Distributions

First we tested our method with Gaussian distributions for the simple reason that they are the easiest for our test. Since our analysis is based on a shape comparison and our shift is horizontal the higher the order and the more rapidly varying our curve is the better. If we have two curves that are almost constant (a straight horizontal line) we would never be able to measure a horizontal shift, because our test measures the vertical distance between this two curves (Fig. 3.2) and the distance between them would not change with the shifts. That is not the case with Gaussians, since is has two clear "ramp up" and "ramp down" portions that make the applied shift very apparent, while still being very simple (in contrast with polynomials, for example).

To produce Figure 3.3 and 3.4 we used 50 thousand events and a step of 0.25 (so for each iteration the shifted distribution was moved by increments of 0.25) while varying the number of bins in the distribution. Figure 3.4 shows the found shift size for the 20 experiments used in this run of the code and Figure 3.3 shows the probability plots for one of these experiments. In these plots we can observe that the binned test usually gives higher probabilities. But if the number of bins is increased its result approaches the result of the unbinned test. In Figure 3.5 we can see an example of the original distributions, the one that stayed fixed through the test and the one that was generated with a shift and will be shifted for the test, as well as the distribution that the test selected from the set of shifted spectra as the most similar. From the distributions we can observe a pretty obvious result of increasing the number of bins while the number of events are fixed, we get bigger uncertainties. In this case we would benefit of having more events to fill up the bins.

In Figures 3.6, 3.7 and 3.8 the number of bins is fixed at 250 and kept the step of 0.25 and varied the number of events. It is clear from Figure 3.6 that for more events the peaks become sharper and a result of that is that the selection of the right shift becomes a lot more precise, since they get closer to the right answer with smaller uncertainties, a feature that can be observed in Fig. 3.7. Figure 3.8 makes evident the importance of having enough events to fill the distributions, so we have enough statistics to perform the test with a good resolution.

For the next Figures 3.9 and 3.10 we can see the effect of different step sizes on the final result. From the figures it is easy to observe that we need a sufficiently small step in order to have enough resolution. That way we can find bigger probabilities values (Fig. 3.9) and have a more precise measurements of the shift magnitude, with less oscillations and smaller uncertainties (Fig. 3.10).

It is clear that the method was able to measure the right value for the shift. And we could also develop an intuition about what choices to make about binning and size of the shifts. So for the next phase we used the Landau Distribution, because it is more similar to the real energy distributions that we will be comparing for this analysis.

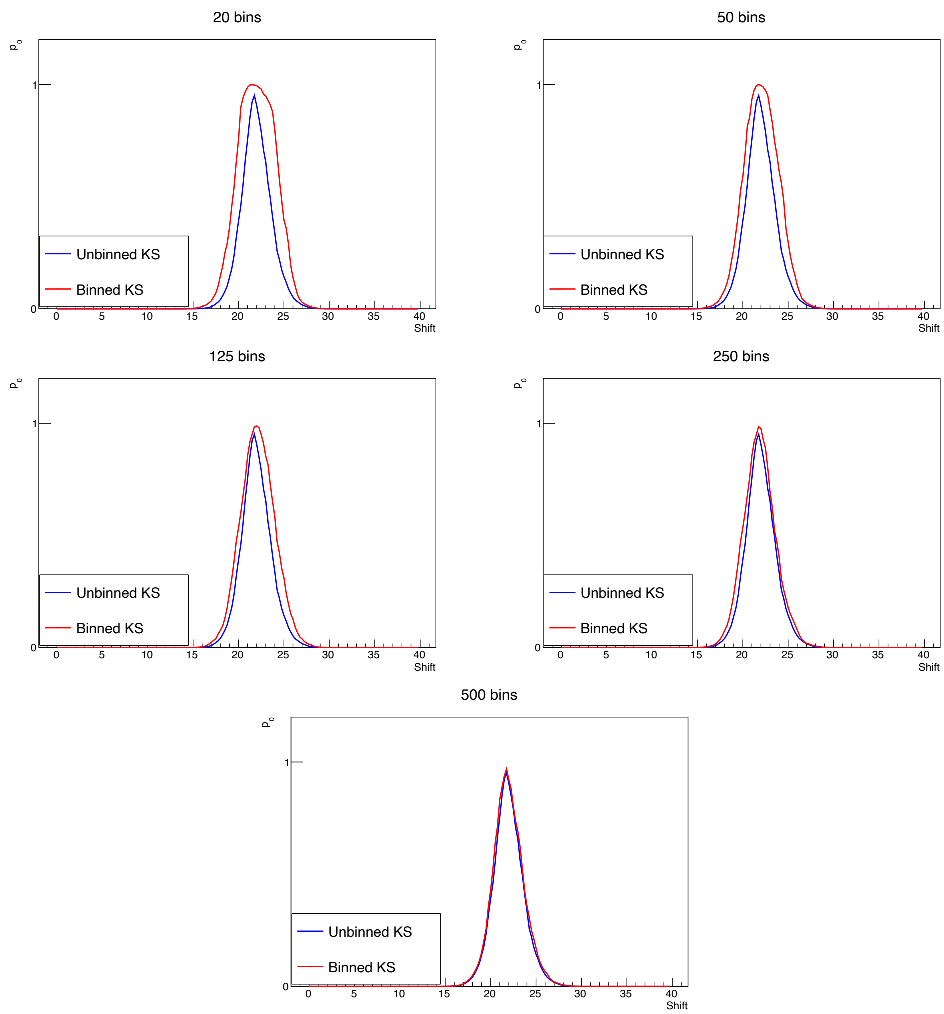

Figure 3.3: An example of probability curves for the binned and unbinned test applied to Gaussian distributions. The number of events and the step are fixed in 50 thousand and 0.25 respectively while the number of bins is varied.

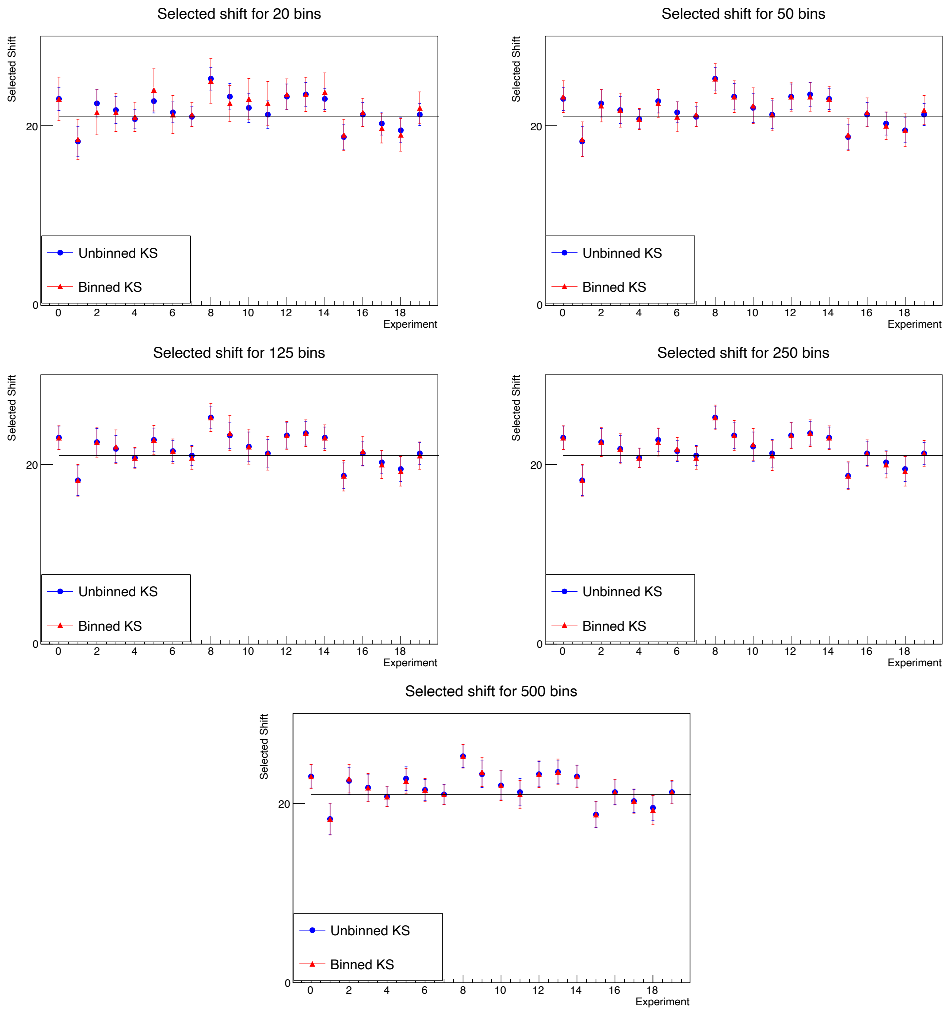

Figure 3.4: Shift size found for binned and unbinned Kolmogorov test applied to Gaussian distributions. 50 thousand events and a step of 0.25 were used. Each point is one experiment and the number of bins varies from 20 in the first one and 500 in the last one. The black horizontal line is the shift magnitude used to generate the shifted distribution, so this is the shift size that the test should find.

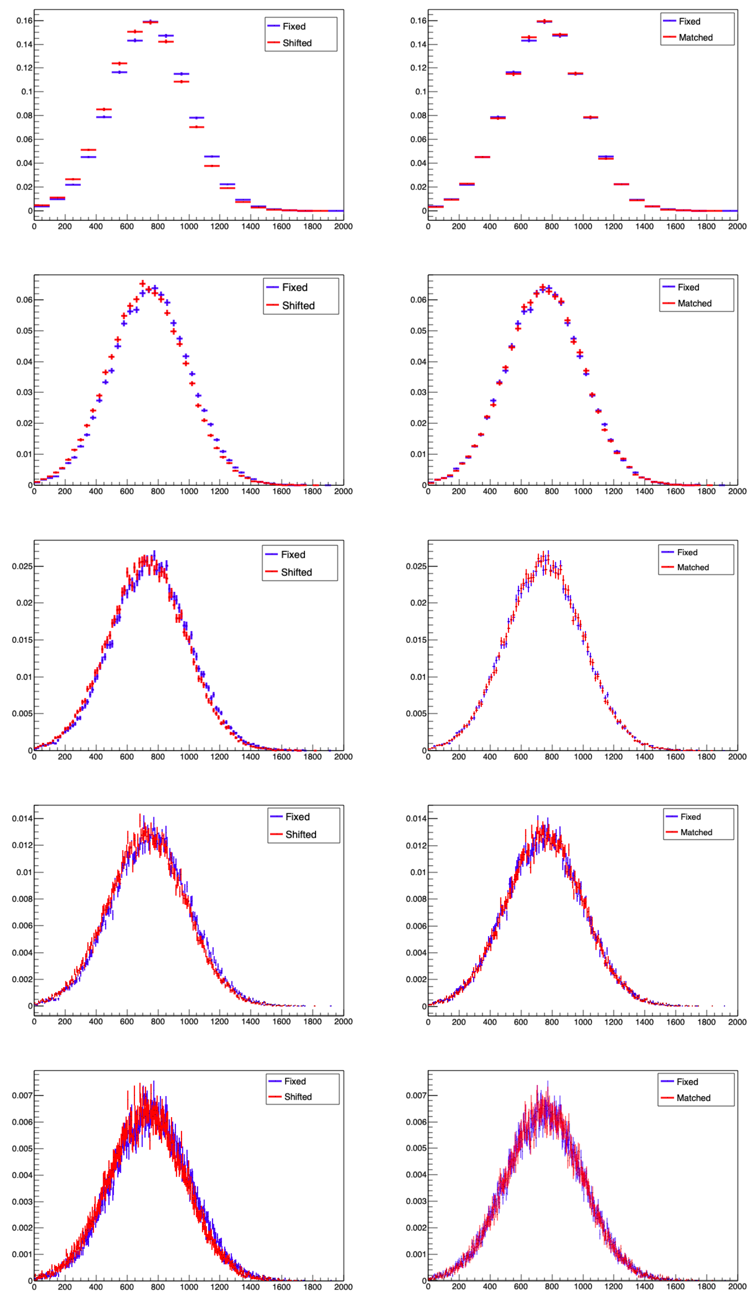

Figure 3.5: On the left we have the energy spectra for both original distributions, the one that will stay fixed and the one that will be shifted for the test. On the right we have the energy spectra for the distribution that stayed fixed and the selected match from the shifted distributions. From top to bottom the number of bins is changed starting with 20 bins, then 50, 125, 250 and 500 bins.

Landau Distributions

The next pictures will follow the same logic at the previous. We used the knowledge acquired with the Gauss distribution tests and made small tweaks to assess the performance of the test when using distributions that are more similar to the real data that we will be using in the analysis.

We start by fixing the number of events at 250 thousand (for better statistics), and the shift at 0.25 (since the smaller the step the better) while varying the number of energy bins. This experiment is pictured in Figures 3.11, 3.12 and 3.13. In this case they all behave the same way the Gaussian distributions did.

The next test is to fix the number of bins and the step size and vary the number of events. We increased a little bit the number of events from the Gaussian case and used 125 energy bins instead of 250 since we could see in the last case that they were already good enough. In Figure 3.14 we can see a huge difference with the increase of statistics. Figures 3.15 and 3.16 also show improvements but not as drastic.

Lastly we test the different sizes of shift for the Landau Distributions. Again the Landau distribution behaves similarly to the Proof of Concept for the Gaussian distrubution. From these test we can conclude that for our method to work we need:

1. To have a big sample of data, so we have enough statistics
2. To bin the energy in a big enough number of bins so the binned Kolmogorov Test gives approximately the same result as the unbinned test, but not so many that we start losing too much statistics and the uncertainties grow.
3. A small enough step (but not too small, because the smaller the step the longer it takes to find the match).

3.6.5 Energy loss measurement

The process of extracting the quark energy loss measurement starts by having two distributions that we want to compare. In practice, what our shape analysis described in

Section 3.6 does is to produce $N + 1$ distributions, where N is the number of shifts performed.

The way the shift is introduced is event by event. That means that, since the acceptance correction is done bin by bin, we have to do the shifting before the acceptance. Then we calculate the acceptance correction, fit, generate the corrected distributions and compare all $N + 1$ distributions like we did in Section 3.6.4. From each probability curve we chose the shift size with the highest probability value as our energy loss. The sigma of our probability curve gives statistical uncertainty of the measurement. This is done for all ν bins and the results are presented in the next chapter.

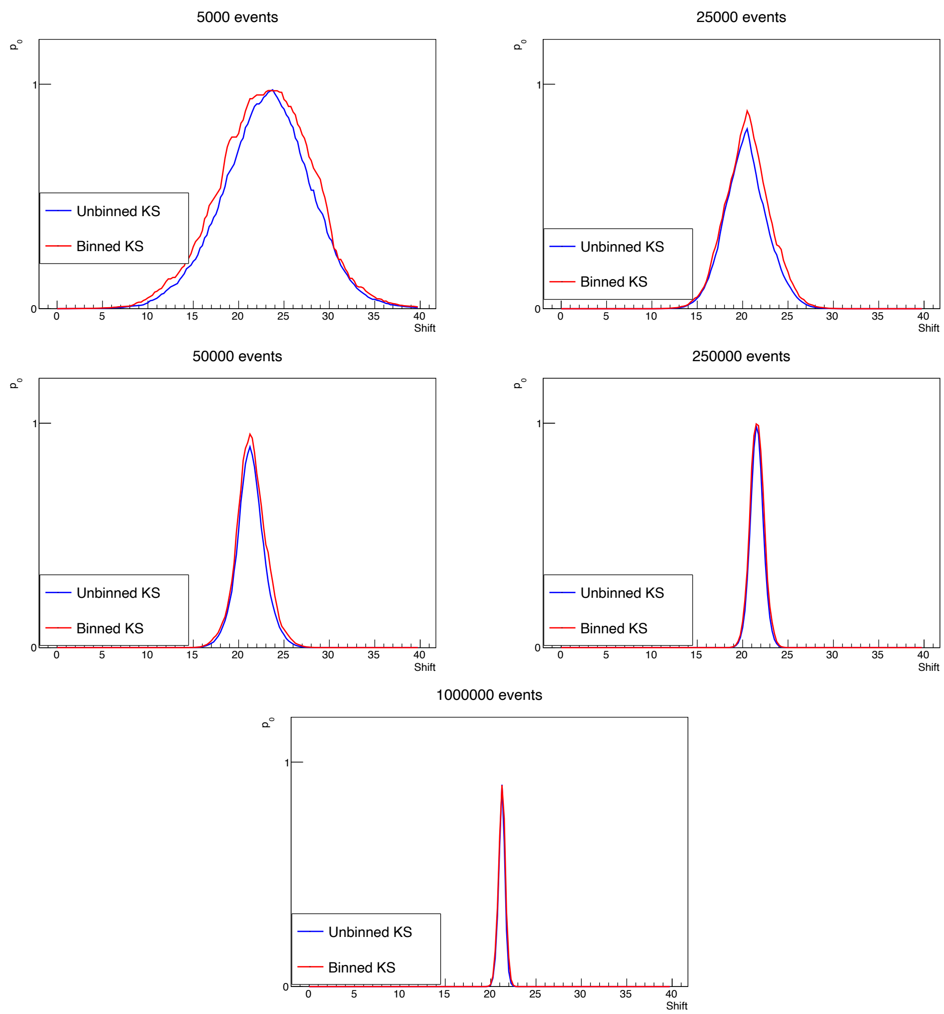

Figure 3.6: An example of robability curves for the binned and unbinned test applied to Gaussian distributions. The number of bins and the step are fixed in 250 and 0.25 respectively while the number of events is varied.

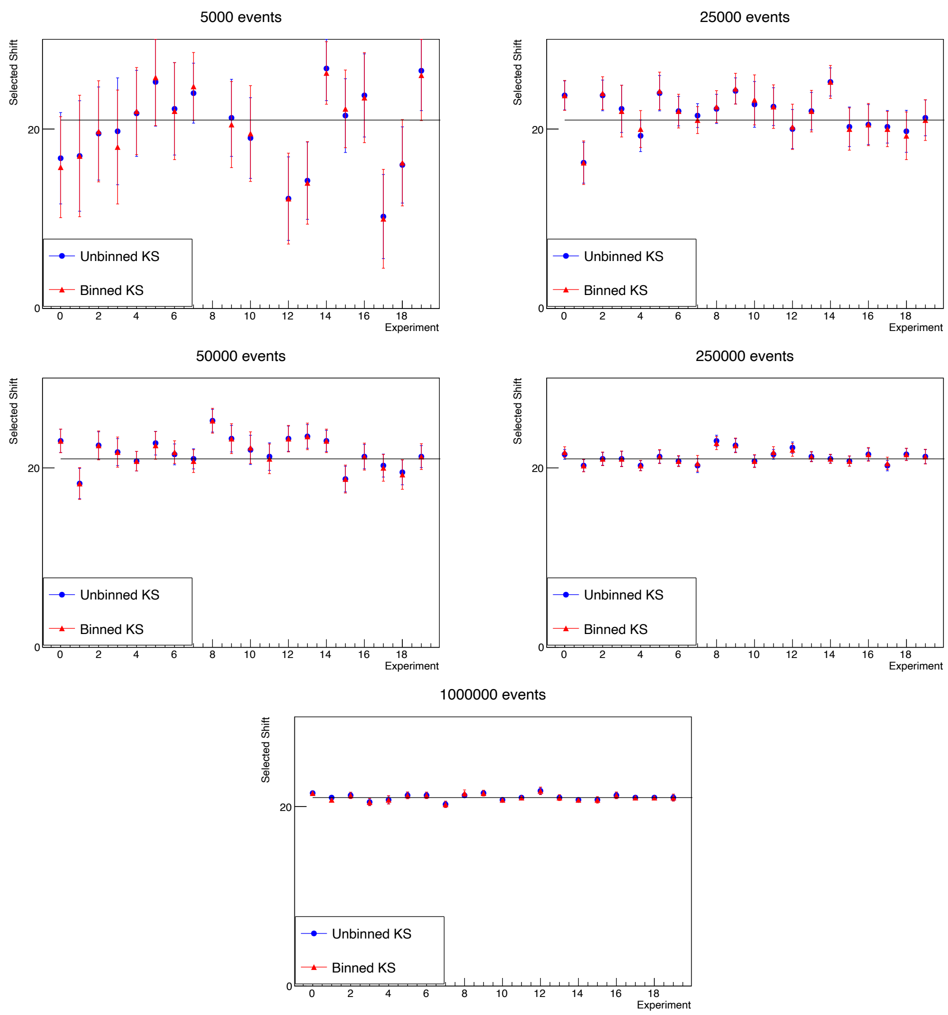

Figure 3.7: Shift size found for binned and unbinned Kolmogorov test applied to Gaussian distributions. 250 bins and steps of 0.25 were used. Each point is one experiment and the number of events varies from 5000 in the first one and 1M in the last one. The black horizontal line is the shift magnitude used to generate the shifted distribution, so this is the shift size that the test should find.

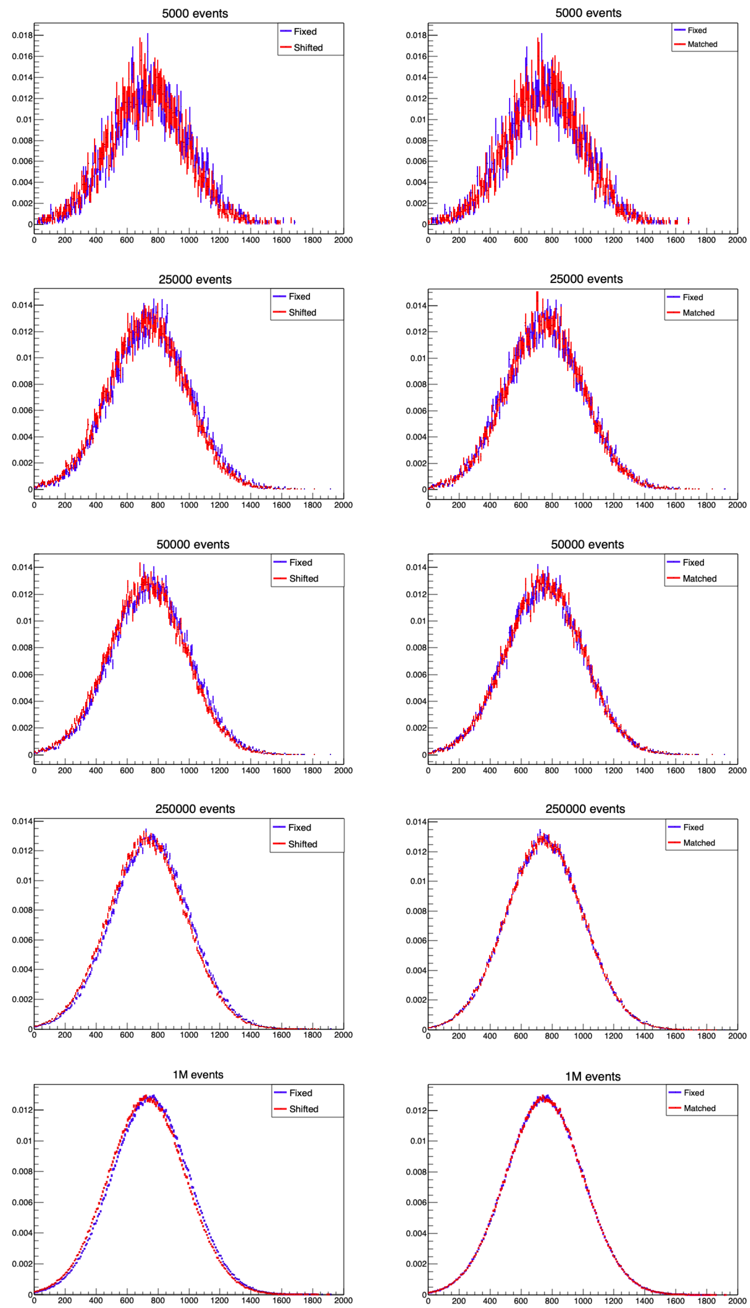

Figure 3.8: On the left we have the energy spectra for both original distributions, the one that will stay fixed and the one that will be shifted for the test. On the right we have the energy spectra for the distribution that stayed fixed and the selected match from the shifted distributions. From top to bottom the number of events is changed.

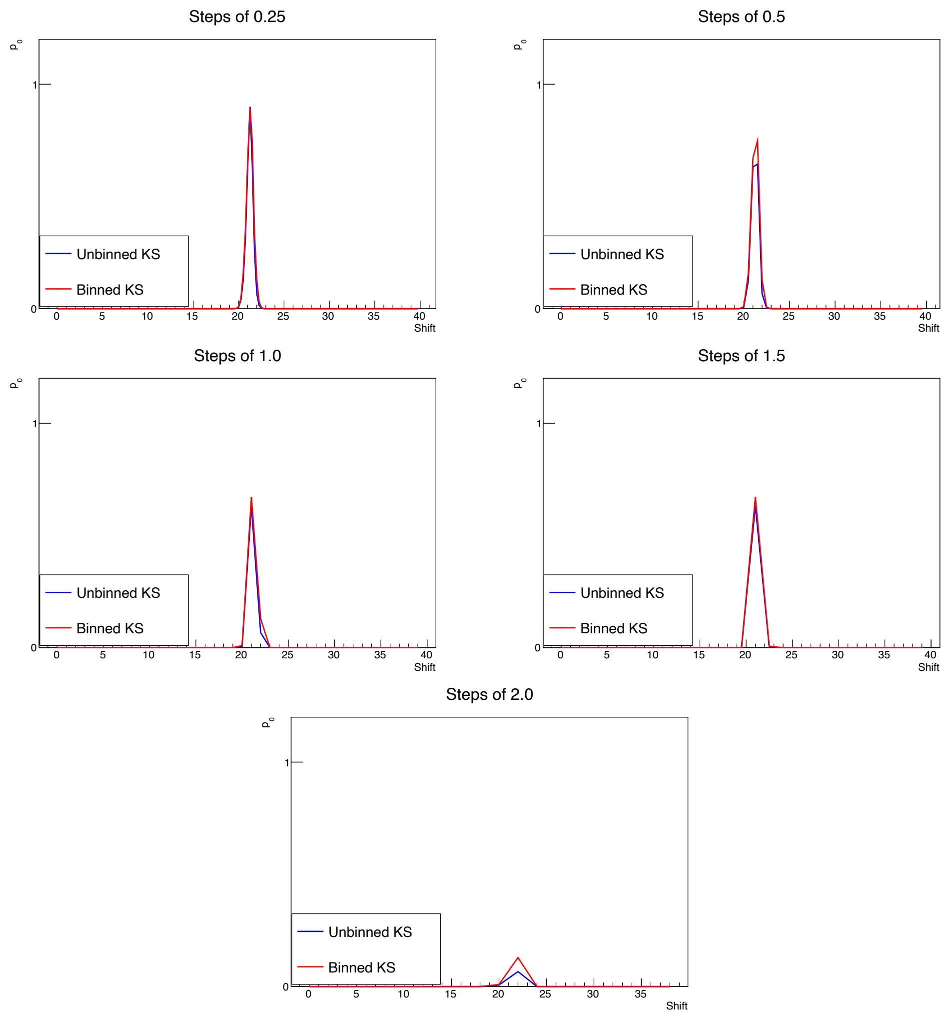

Figure 3.9: An example of probability curves for the binned and unbinned test applied to Gaussian distributions. The number of events and the number of bins is fixed in 1 Million and 250 bins, respectively while the size of the step if varied.

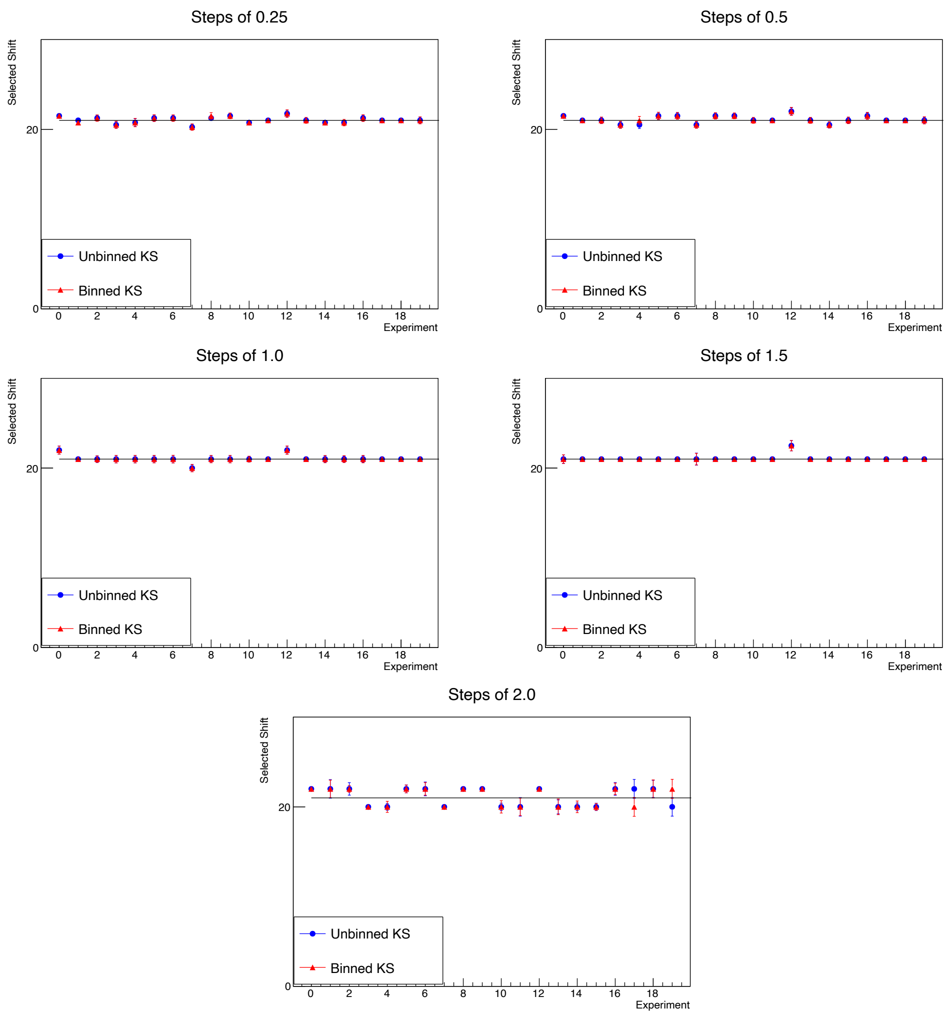

Figure 3.10: Shift size found for binned and unbinned Kolmogorov test applied to Gaussian distributions. 1M thousand events and 250 bins were used. Each point is one experiment and the size of the step used varies from 0.25 in the first one and 2.0 in the last one.

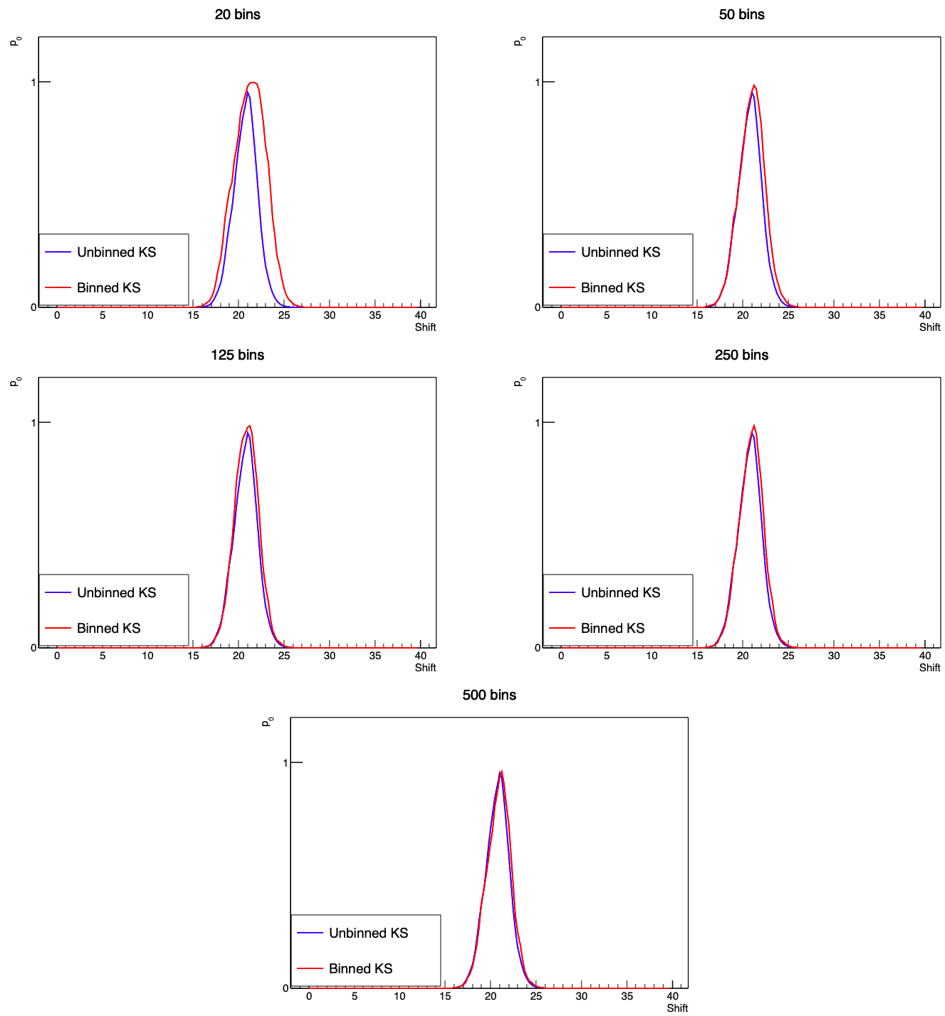

Figure 3.11: An example of probability curves for the binned and unbinned test applied to Landau distributions. The number of events and the step are fixed at 250 thousand and 0.25 respectively while the number of bins is varied.

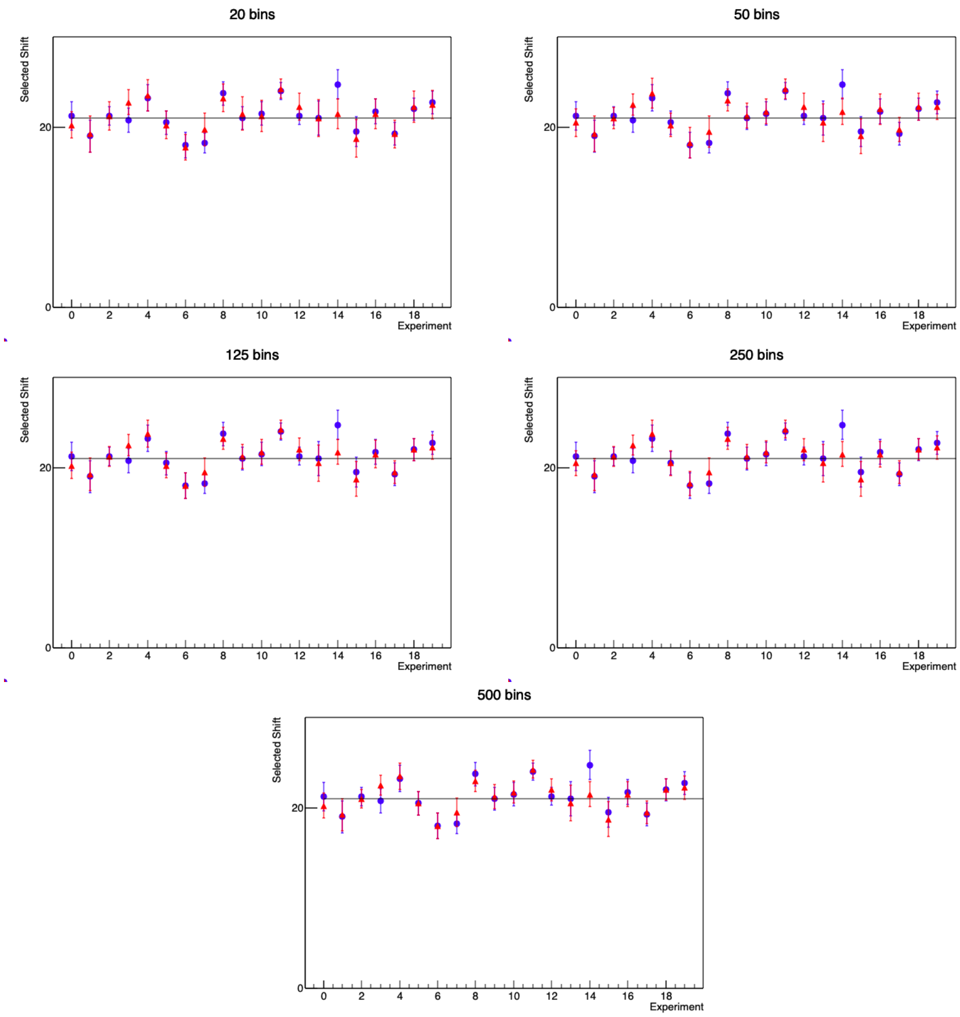

Figure 3.12: Shift size found for binned and unbinned Kolmogorov test applied to Landau distributions. 250 thousand events and a step of 0.25 was used. Each point is one experiment and the number of bins varies. The black horizontal line is the shift magnitude used to generate the shifted distribution, so this is the shift size that the test should find.

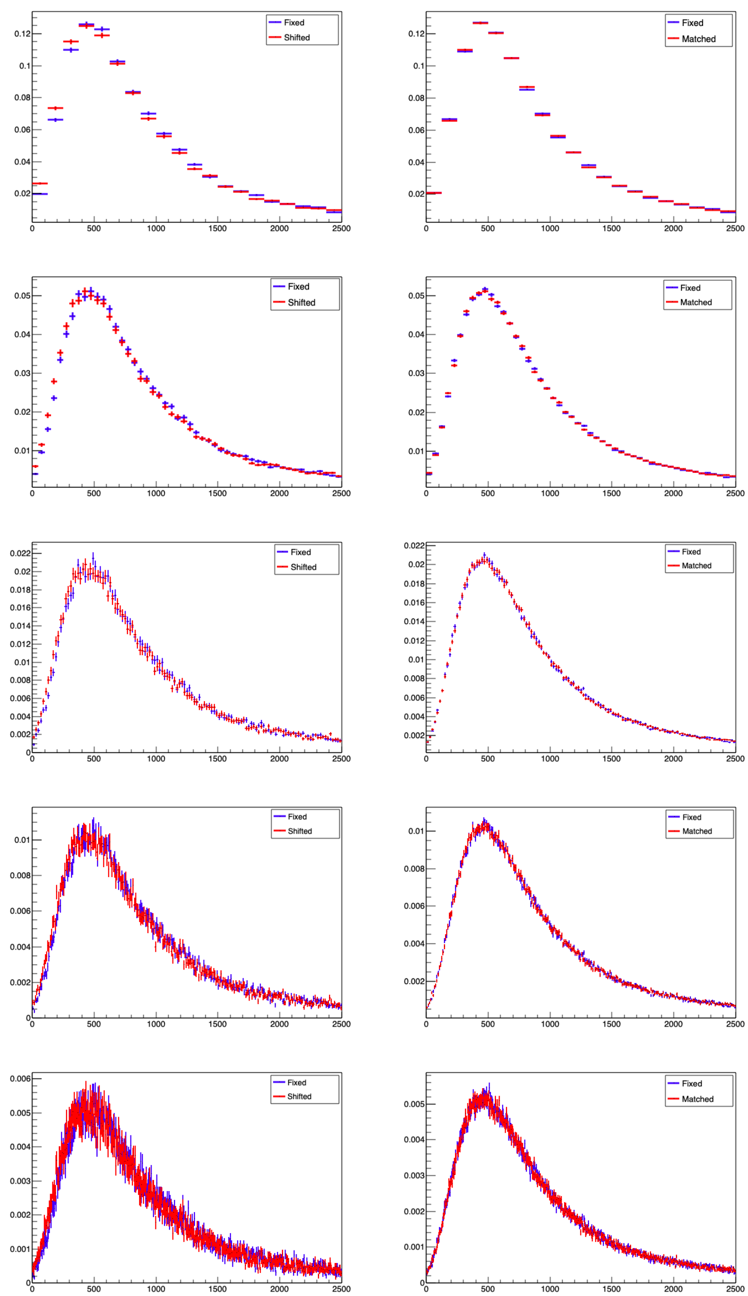

Figure 3.13: On the left we have the energy spectra for both original distributions, the one that will stay fixed and the one that will be shifted for the test. On the right we have the energy spectra for the distribution that stayed fixed and the selected match from the shifted distributions. From top to bottom the number of bins is changed starting with 20 bins, then 50, 125, 250 and 500 bins.

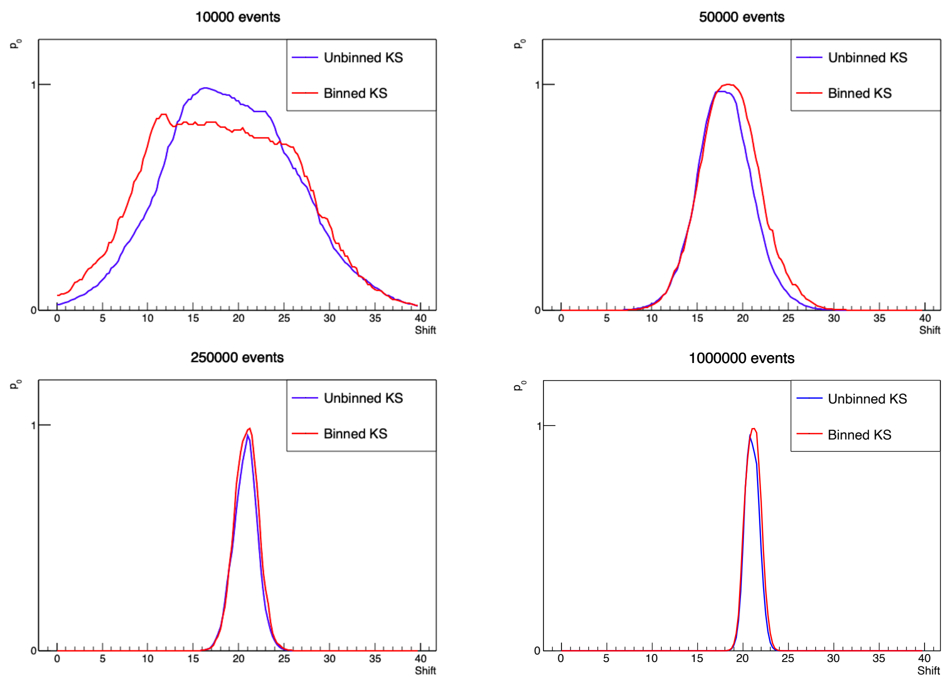

Figure 3.14: An example of probability curves for the binned and unbinned test applied to Landau Distributions. The number of energy bins and the step are fixed at 125 thousand and 0.25 respectively while the number of events is varied.

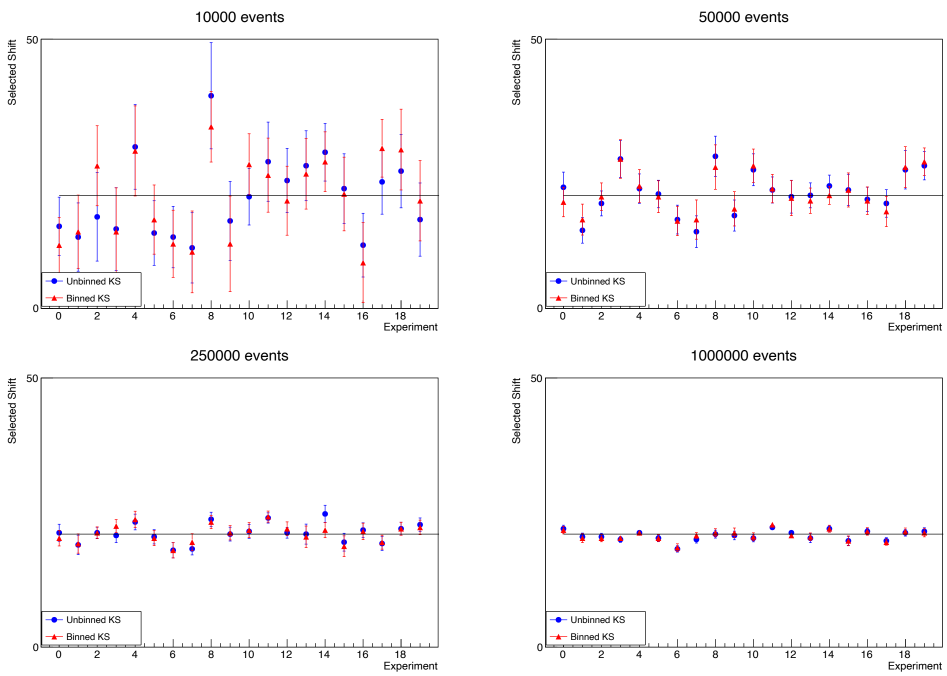

Figure 3.15: Shift size found for binned and unbinned Kolmogorov test applied to Landau distributions. 125 energy bins and a step of 0.25 were used. Each point is one experiment and the number of events varies. The black horizontal line is the shift magnitude used to generate the shifted distribution, so this is the shift size that the test should find.

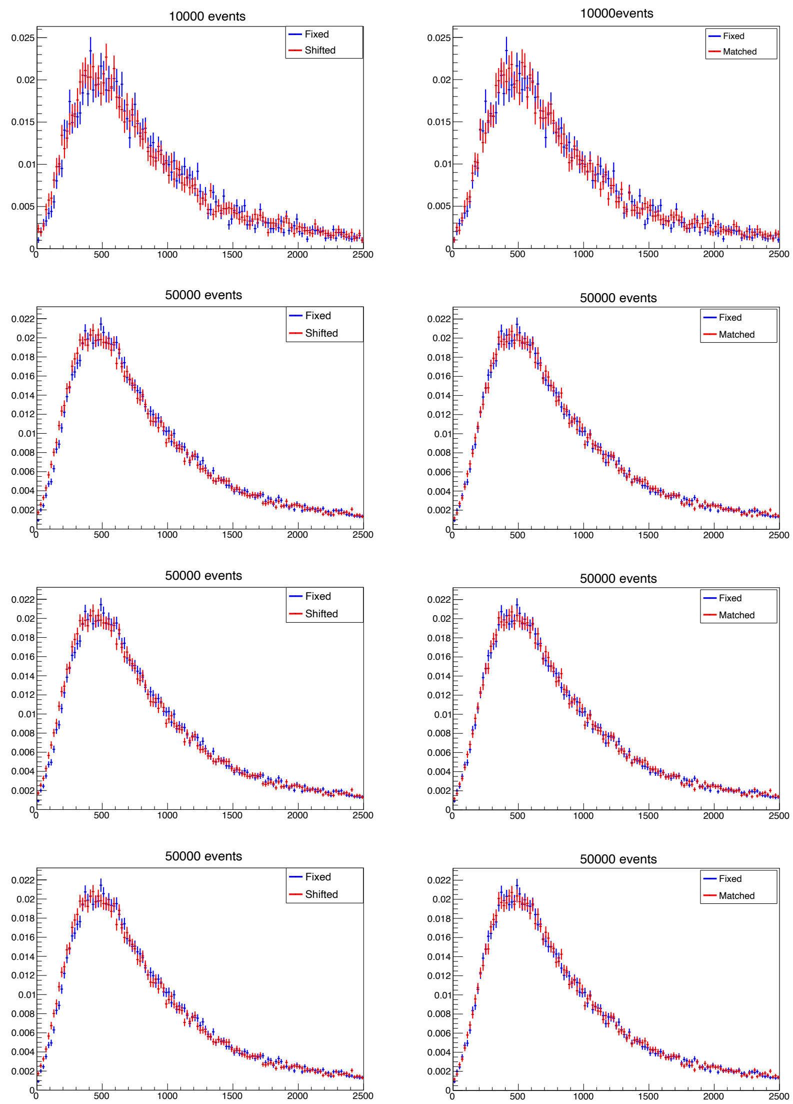

Figure 3.16: On the left we have the energy spectra for both original distributions, the one that will stay fixed and the one that will be shifted for the test. On the right we have the energy spectra for the distribution that stayed fixed and the selected match from the shifted distributions. From top to bottom the number of events is changed.

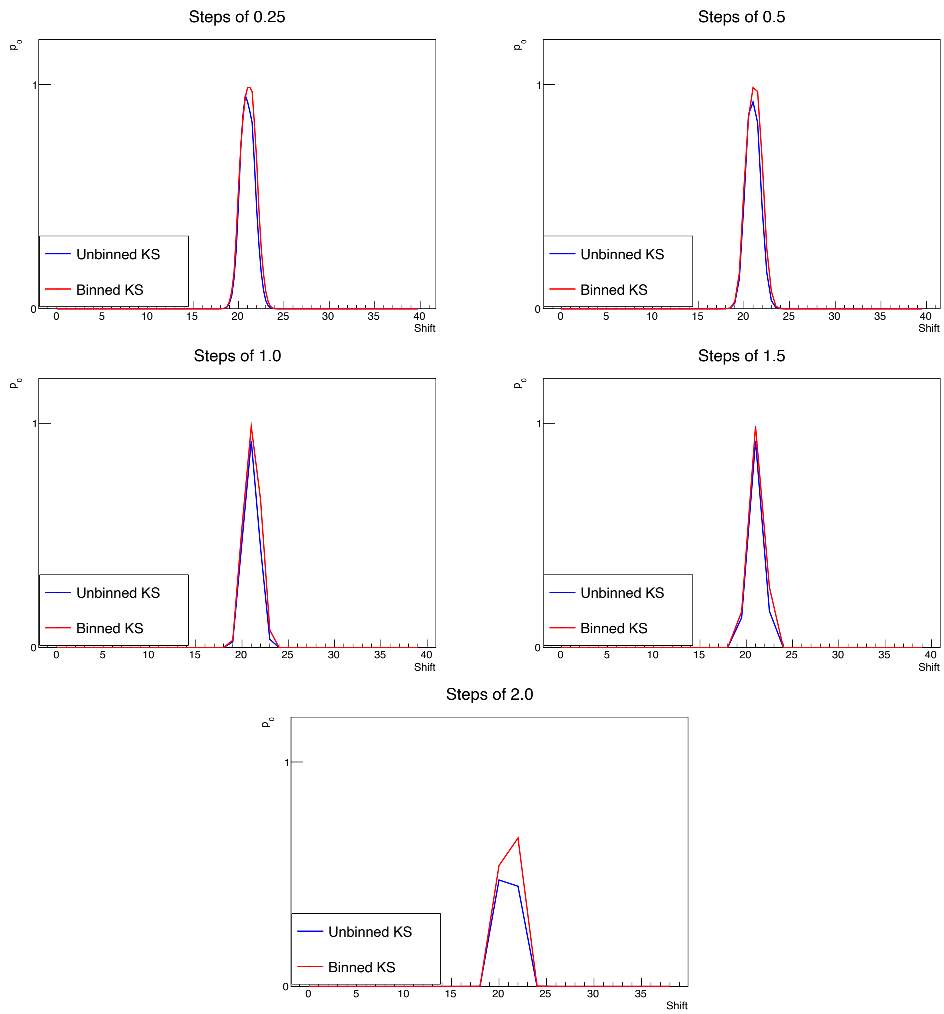

Figure 3.17: An example of probability curves for the binned and unbinned test applied to Landau distributions. The number of energy bins and the step are fixed at 125 thousand and 0.25 respectively while the number of events is varied.

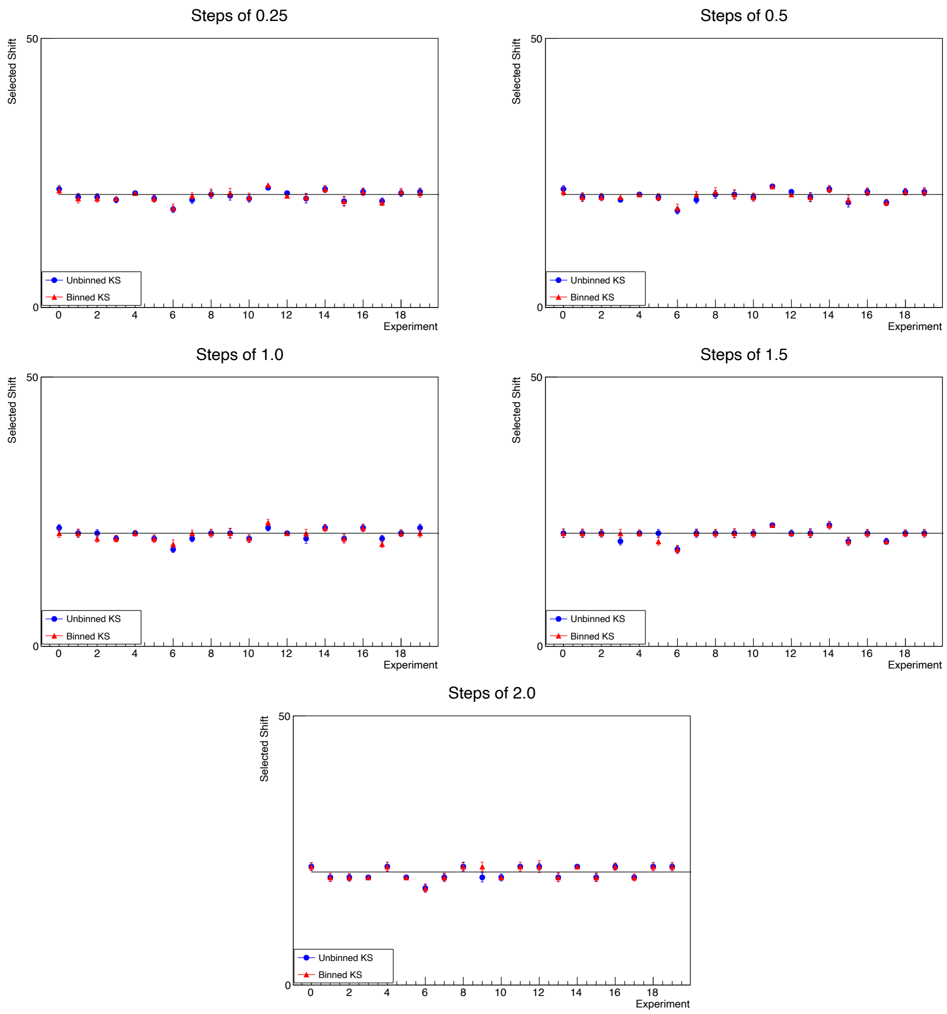

Figure 3.18: Shift size found for binned and unbinned Kolmogorov test applied to Landau distributions. 125 energy bins and 1 million events were used. Each point is one experiment and the number of events varies. The black horizontal line is the shift magnitude used to generate the shifted distribution, so this is the shift size that the test should find.

Chapter 4

Results

This chapter presents the measurement of quark energy loss for all three targets in ν bins. There are results for acceptance corrected data in one and two dimensions. For all cases we used δE steps of 1 MeV and 125 energy bins for the TH1F Kolmogorov-Smirnov test, the binned test.

The nu bins used are described in Table 4.1. For each target we will show the probability curves with and without acceptance correction as well as the matching of the distributions. For the 2D acceptance corrections case the variable used is Q^2 binned in the manner shown in Table 4.2. Figures 4.1 and 4.2 show examples of the acceptance fits used for the corrections.

Nu bin	Nu range
0	3.2 < Nu < 3.4
1	3.4 < Nu < 3.6
2	3.6 < Nu < 3.8
3	3.8 < Nu < 4.0
4	4.0 < Nu < 4.2

Table 4.1: Nu bins.

Q^2 bin	Q^2 range
1	$1.0 < Q^2 < 1.5$
2	$1.5 < Q^2 < 2.0$
3	$2.0 < Q^2 < 2.5$
4	$2.5 < Q^2 < 3.0$
5	$3.0 < Q^2 < 3.5$
6	$3.5 < Q^2 < 4.0$

Table 4.2: Q^2 bins for the 2D acceptance corrections.

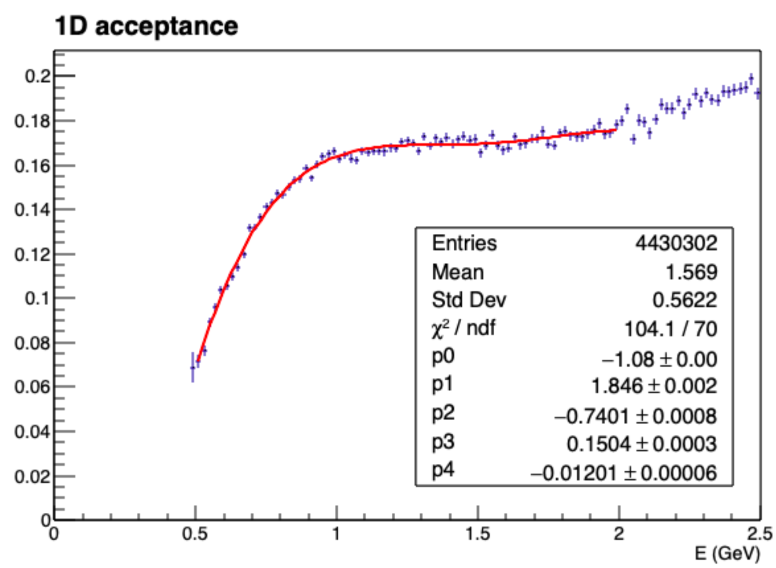

Figure 4.1: Example of 1D acceptance correction fit for deuterium target.

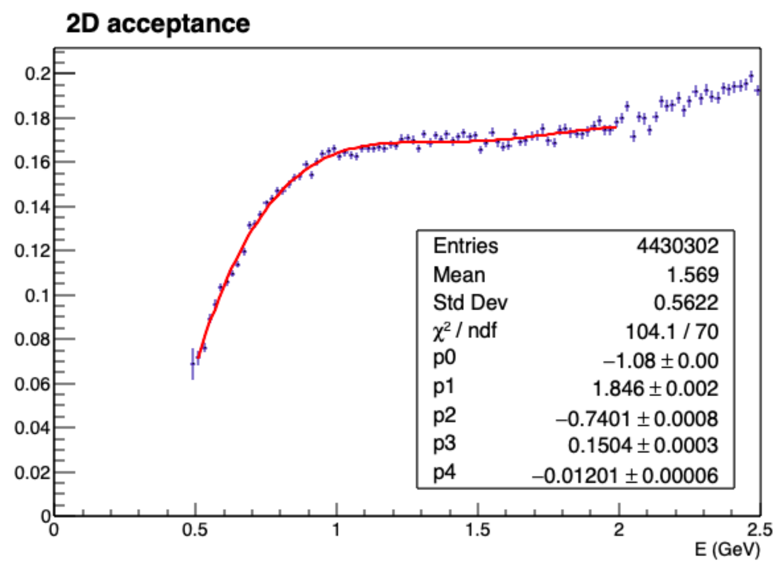

Figure 4.2: Example of 2D acceptance correction fit for deuterium target.

4.1 Carbon

Figure 4.3, 4.4, 4.5 and 4.6 show the results for the carbon target with 1D acceptance corrections compared with the uncorrected data. The probability curves in Fig. 4.3 show a tendency of finding bigger energy loss for corrected data and the drop in energy loss with bigger nu seen in 4.6 is not expected.

Figures 4.7, 4.8 and 4.9 compare the results from the carbon target with 2D acceptance corrections, with the previous results. The probability magnitudes are slightly smaller and Fig. 4.8 evidences that: where we can see that the nu bins with the smallest probabilities (nu bin 0 and 2) are also the ones that have the worse match between distributions when compared to the match for the 1D acceptances . Not only that, a further increase in energy loss can be seen after the 2D correction. Besides, the drop in the energy loss for bigger ν observed for 1D acceptances appears to have suffered a slight suppression.

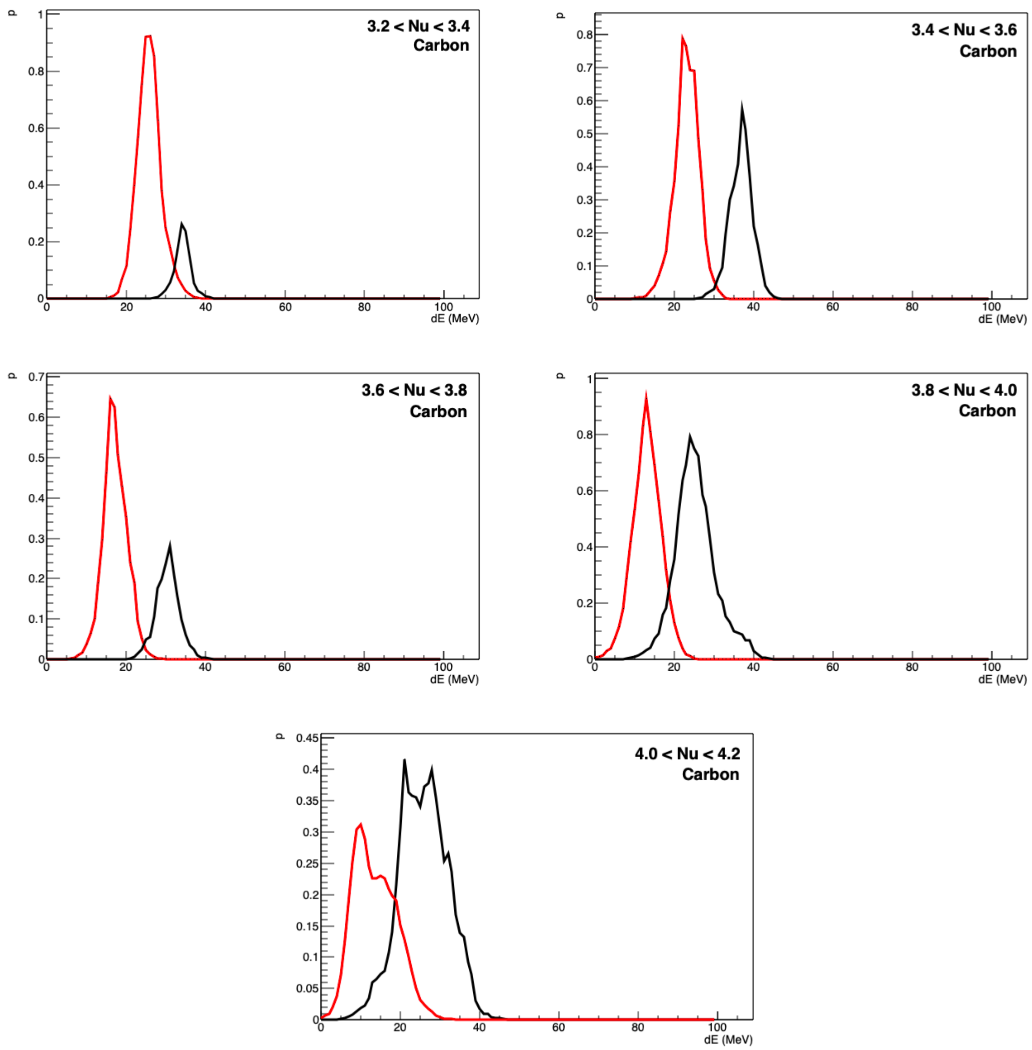

Figure 4.3: Probability values of binned KS-test for the carbon target as a function of the energy shift. The red line is the uncorrected data and the black line is the 1D acceptance corrected data.

4.2 Iron

For the Iron target, the resulting probability curves for the 1D acceptance corrected data were too small in magnitude to be compared with the uncorrected case, as it can be seen

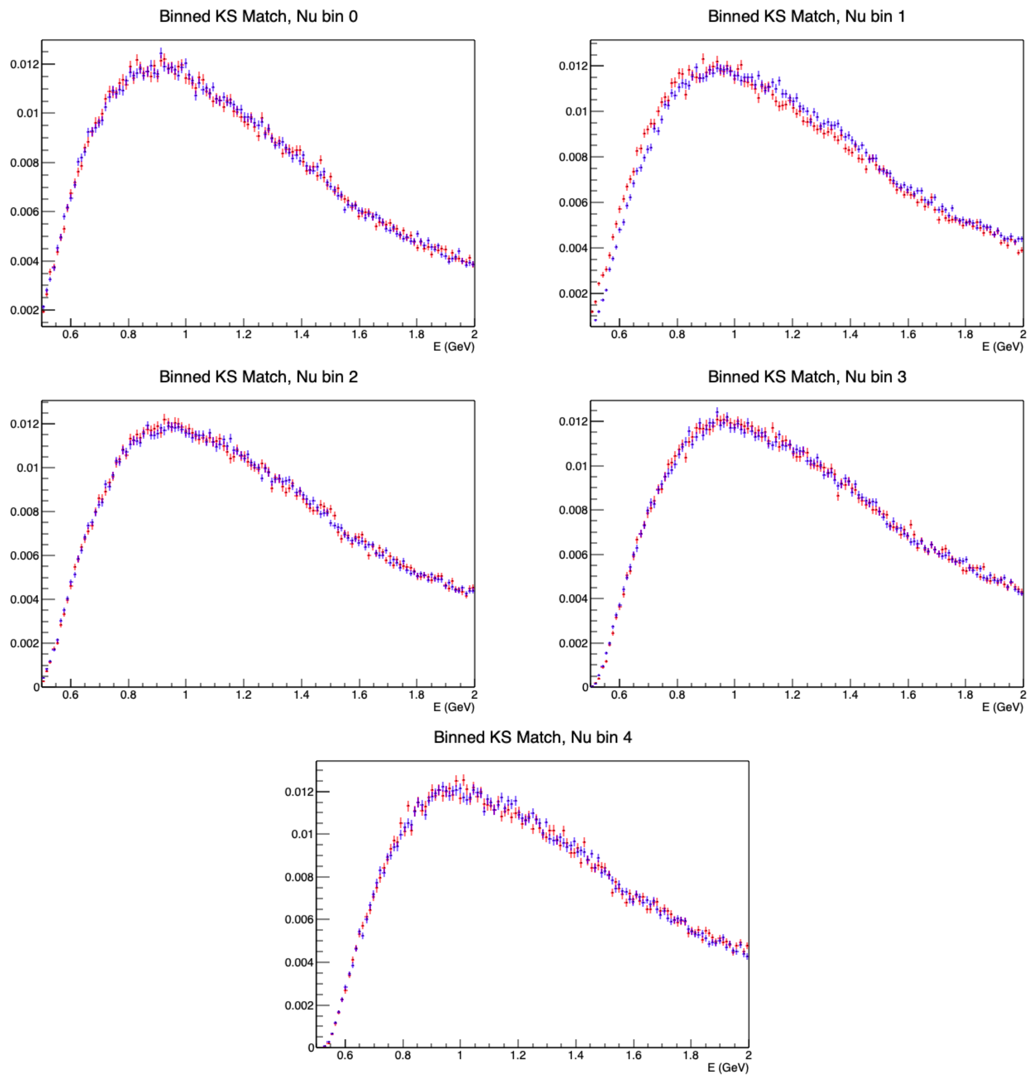

Figure 4.4: Uncorrected pion energy spectra for deuterium (blue) superimposed on the pion energy spectrum for carbon (red) which has been shifted horizontally along the axis by the measured energy loss. The data are normalized to unity for comparison and have no corrections. Error bars represent statistical error only.

in Figure 4.10 and 4.12. The first 3 Nu bins resulted in even smaller probabilities for the 1D acceptance case, which is evident by the matching distributions in Fig. 4.13. Regardless, the test was still able to find a probability distribution and a value for the energy loss.

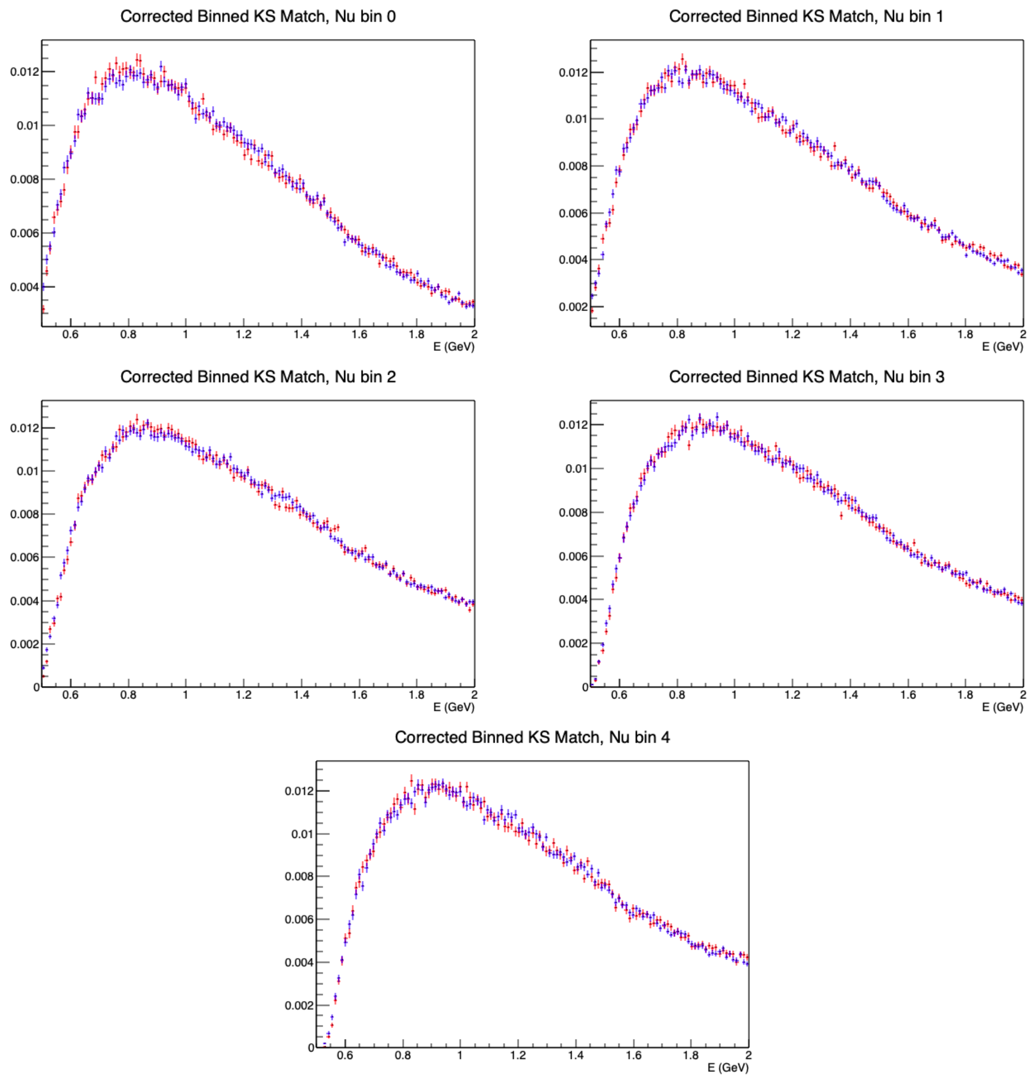

Figure 4.5: Corrected pion energy spectra for deuterium (blue) superimposed on the pion energy spectrum for carbon (red) which has been shifted horizontally along the axis by the measured energy loss. The data are normalized to unity for comparison and corrected with 1D acceptance. Error bars represent statistical error only.

Figure 4.14 shows the comparison between the Kolmogorov test probabilities for data corrected with 1D and 2D acceptances. The match between distributions is worse (Fig. 4.15). The same behavior seen for carbon repeats itself here, the measured energy loss is slightly bigger for the 2D case, although a downward trend in energy loss for

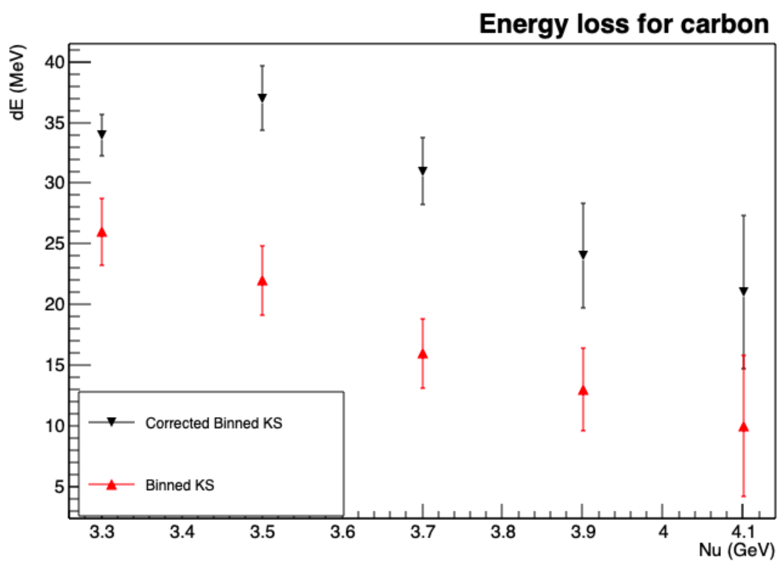

Figure 4.6: Quark energy loss for carbon as a function of ν for 1D acceptance corrected data.

bigger nu is still present. This trend can be partly explained by the fact that we always choose the shift value of the top of the probability curve, but for higher nu bins the curve is asymmetric and the highest value of the probability does not correspond to the centroid of the curve.

4.3 Lead

In the case of lead the probabilities found for the corrected data were also too small in magnitude to be compared with the uncorrected results. Regardless the test still found a peak and a value for the energy loss, as it can be seen in Fig. 4.17 for the uncorrected and 1D acceptance and in Fig. 4.19 for the comparison between 1D and 2D acceptance corrected data. The matching distributions are also worse than for the carbon and iron targets (Fig. 4.18, 4.20 and 4.22). One thing to notice in Fig. 4.17 is that for most cases the probability curve for the 2D acceptance corrected data is bigger than the 1D acceptance corrected data. That means that the acceptance correction improves the

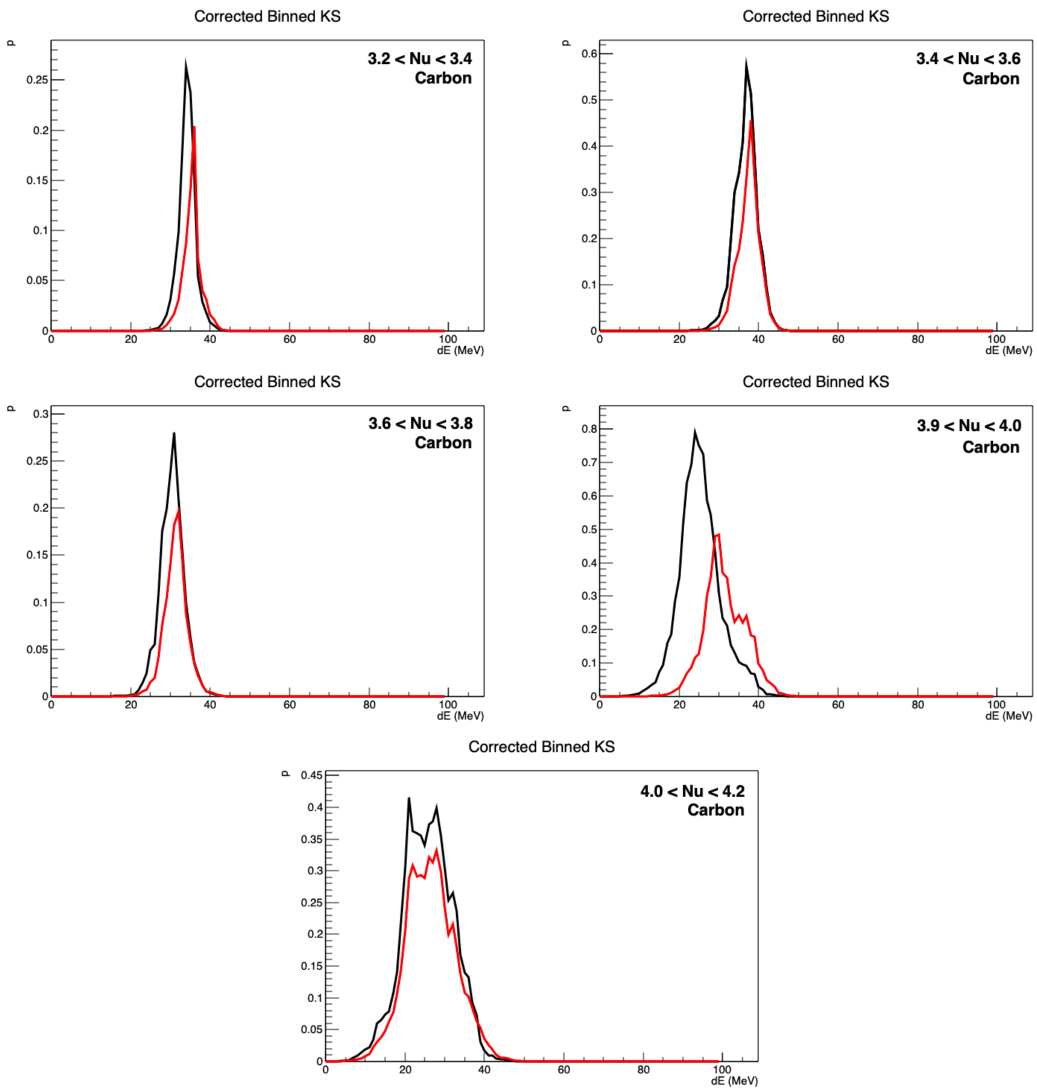

Figure 4.7: Probability values of binned KS-test for the carbon target as a function of the energy shift. Both curves are for the corrected distribution, the black is for 1D acceptance and the red is for 2D acceptance

match.

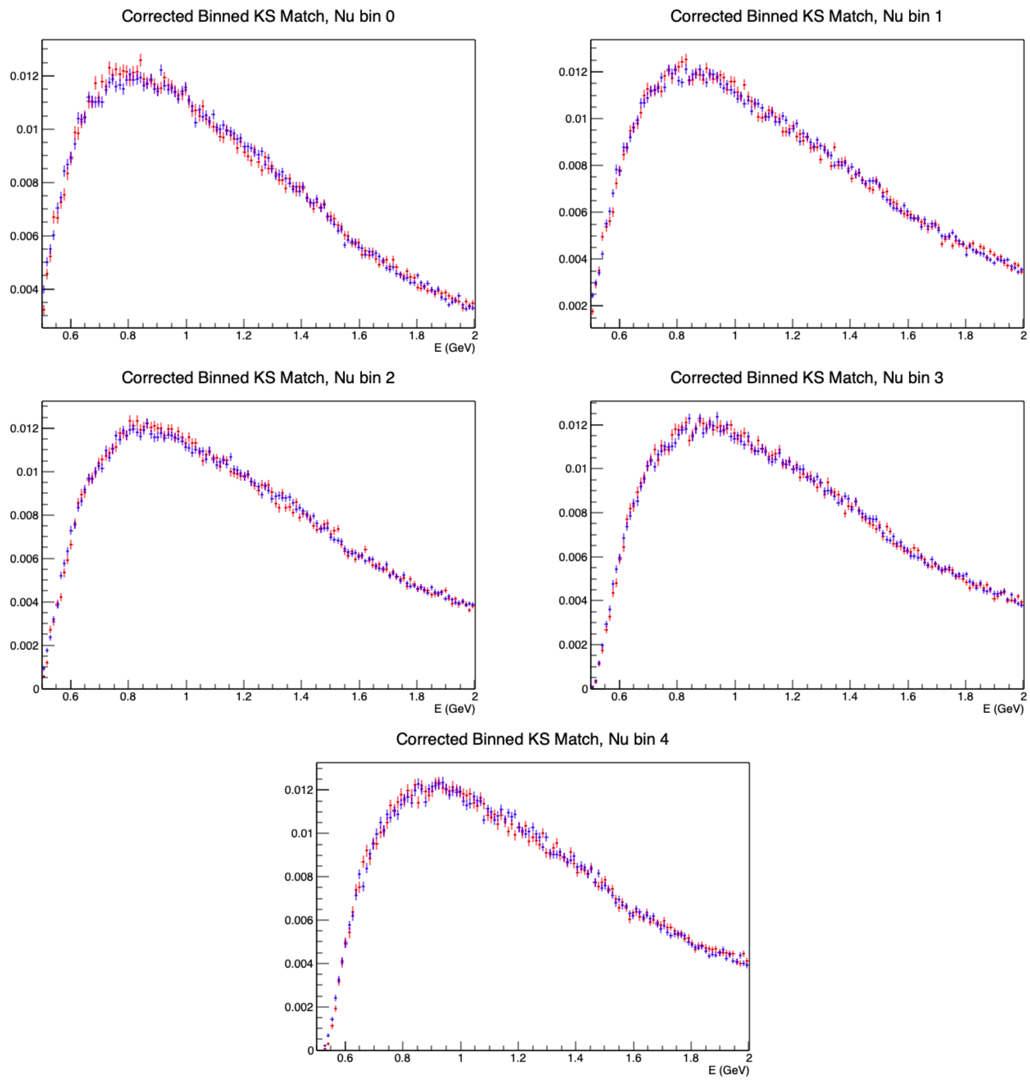

Figure 4.8: Corrected pion energy spectra for deuterium (blue) superimposed on the pion energy spectrum for carbon (red) which has been shifted horizontally along the axis by the measured energy loss. The data are normalized to unity for comparison and corrected with 2D acceptances. Error bars represent statistical error only.

4.4 Comparison

For the final result: Figure 4.24 shows the final measured energy loss for all targets, corrected with 2D acceptance factors, and Figure 4.25 shows the final energy loss for all

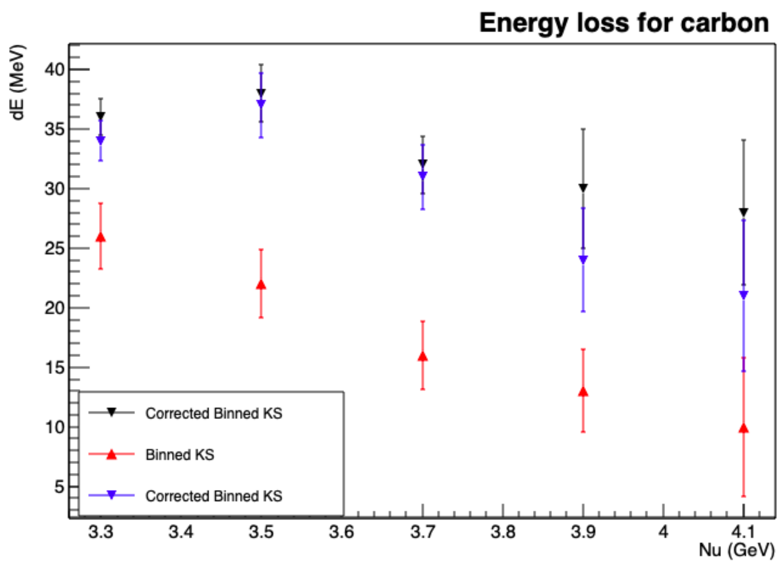

Figure 4.9: Quark energy loss for carbon as a function of ν. The red points represent uncorrected results while the blue and black points are for 1D and 2D acceptance corrected data, respectively.

targets, 2D acceptance corrections and the Coulomb corrections from 3.1. As expected, the bigger the nucleus the more energy loss happens where for lead we have the biggest values for the measurement and the smallest for the carbon. The error bars were defined as the sigma of a fitted Gaussian. Notice that some of the points appear to have no error bars, or very small ones, that is because in those cases the probability curve is very very small, yielding small error bars too.

Nu bin	Carbon	Iron	Lead
3.2 < Nu < 3.4	36 ± 1.51	70 ± 0.73	86 ± 1.57
3.4 < Nu < 3.6	38 ± 2.39	65 ± 0.96	91 ± 1.04
3.6 < Nu < 3.8	32 ± 2.43	69 ± 1.00	77 ± 1.46
3.8 < Nu < 4.0	30 ± 5.00	66 ± 1.57	76 ± 1.76
4.0 < Nu < 4.2	28 ± 6.1	57 ± 2.82	77 ± 2.7

Table 4.3: Energy loss measurement for 1D acceptance corrected data without Coulomb corrections.

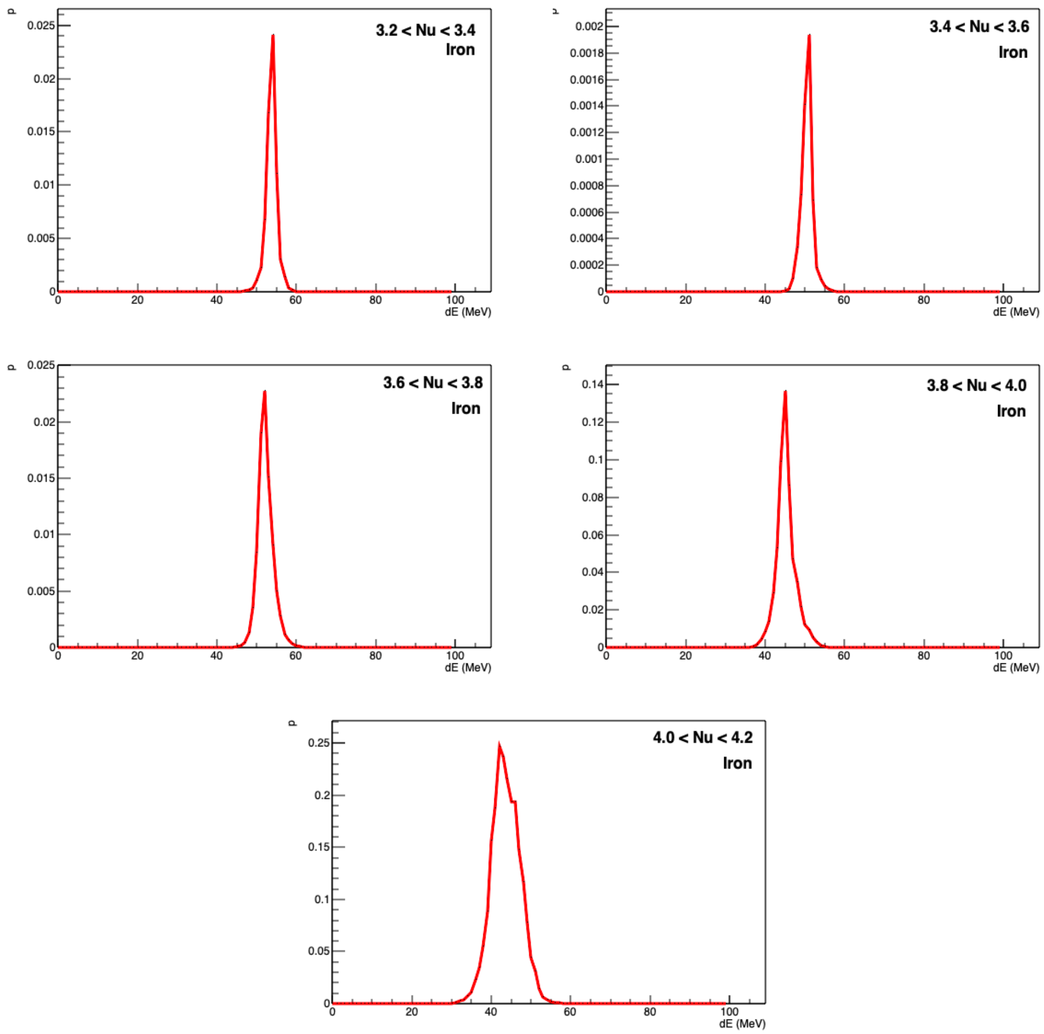

Figure 4.10: Probability values of binned KS-test for the iron target as a function of the energy shift. The plots are for uncorrected data.

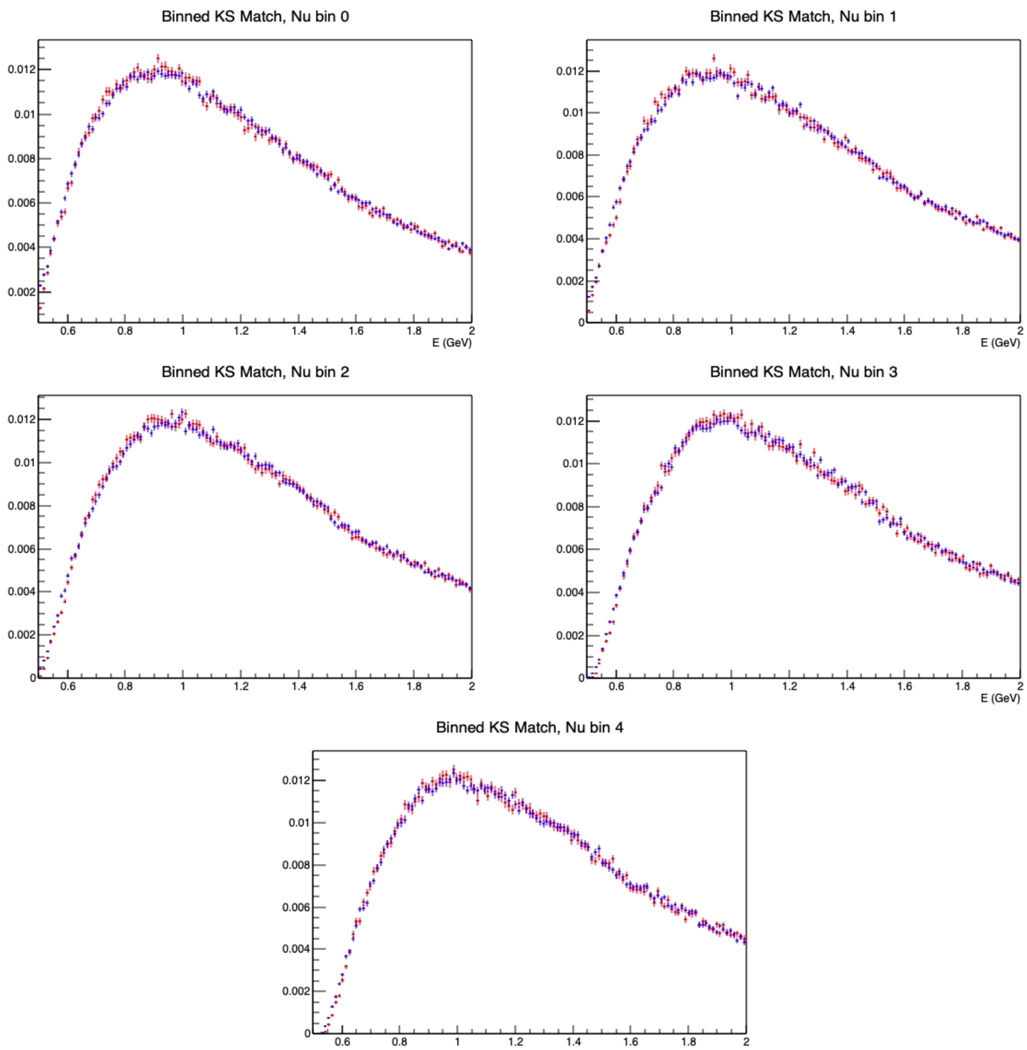

Figure 4.11: Uncorrected pion energy spectra for deuterium (blue) superimposed on the pion energy spectrum for iron (red) which has been shifted horizontally along the axis by the measured energy loss. The data are normalized to unity for comparison and have no acceptance corrections. Error bars represent statistical error only.

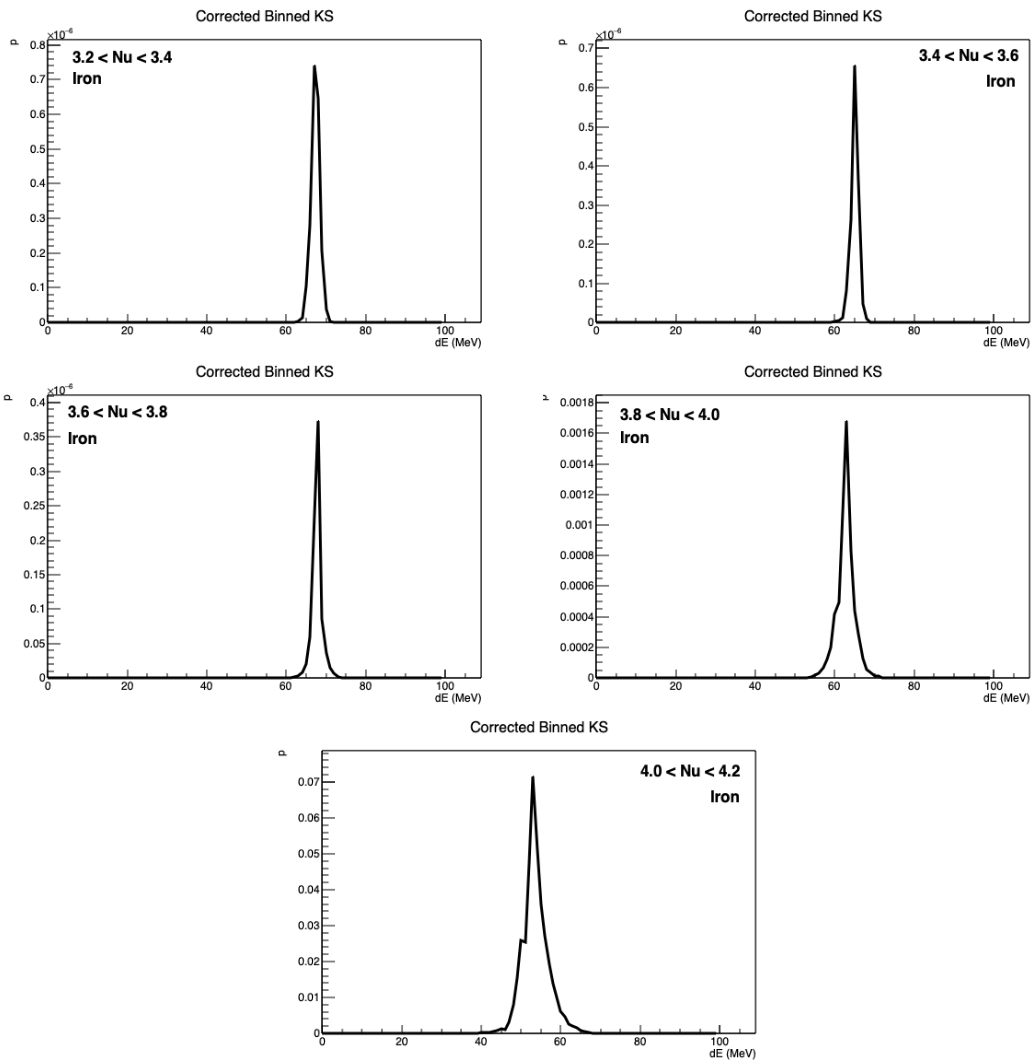

Figure 4.12: Probability values of binned KS-test for the iron target as a function of the energy shift. The plots are for 1D acceptance corrected data.

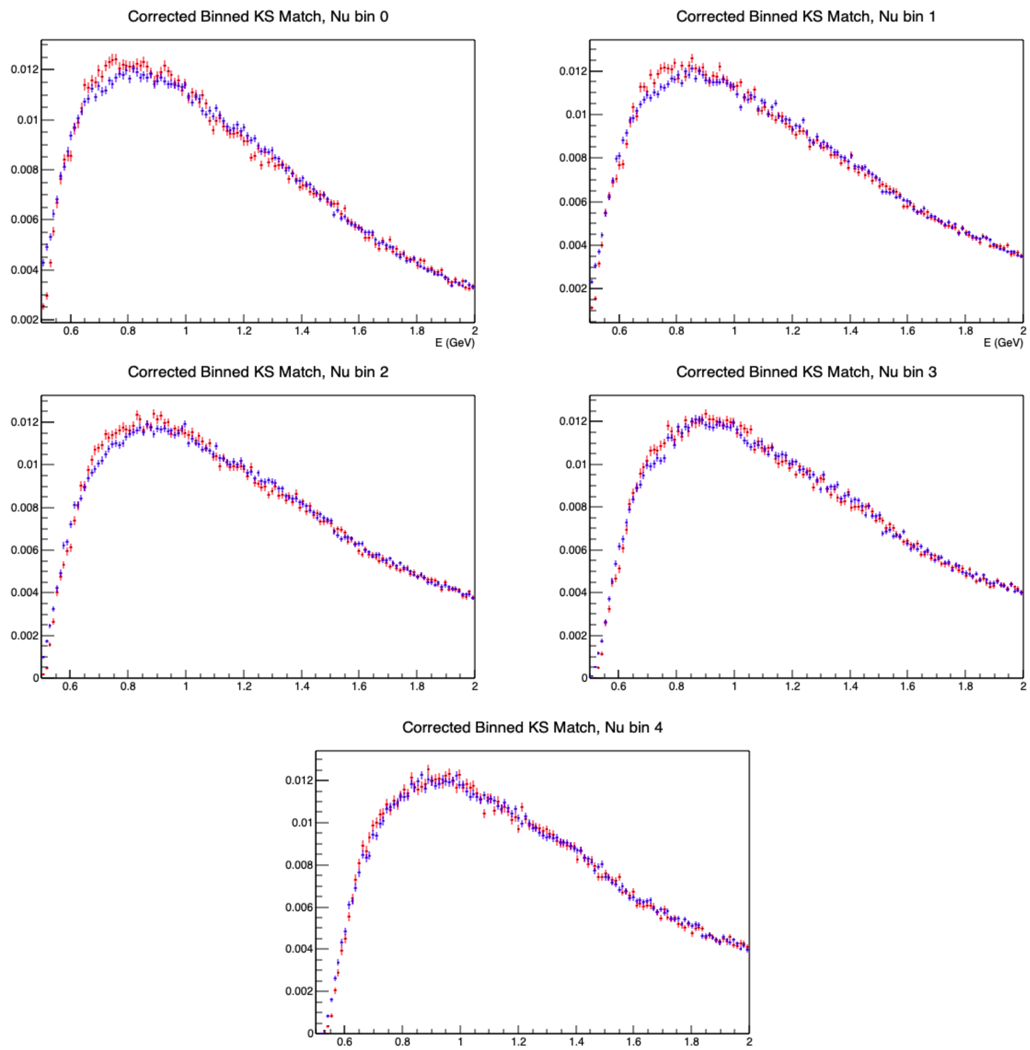

Figure 4.13: Corrected pion energy spectra for deuterium (blue) superimposed on the pion energy spectrum for iron (red) which has been shifted horizontally along the axis by the measured energy loss. The data are normalized to unity for comparison and have 1D acceptance corrections. Error bars represent statistical error only.

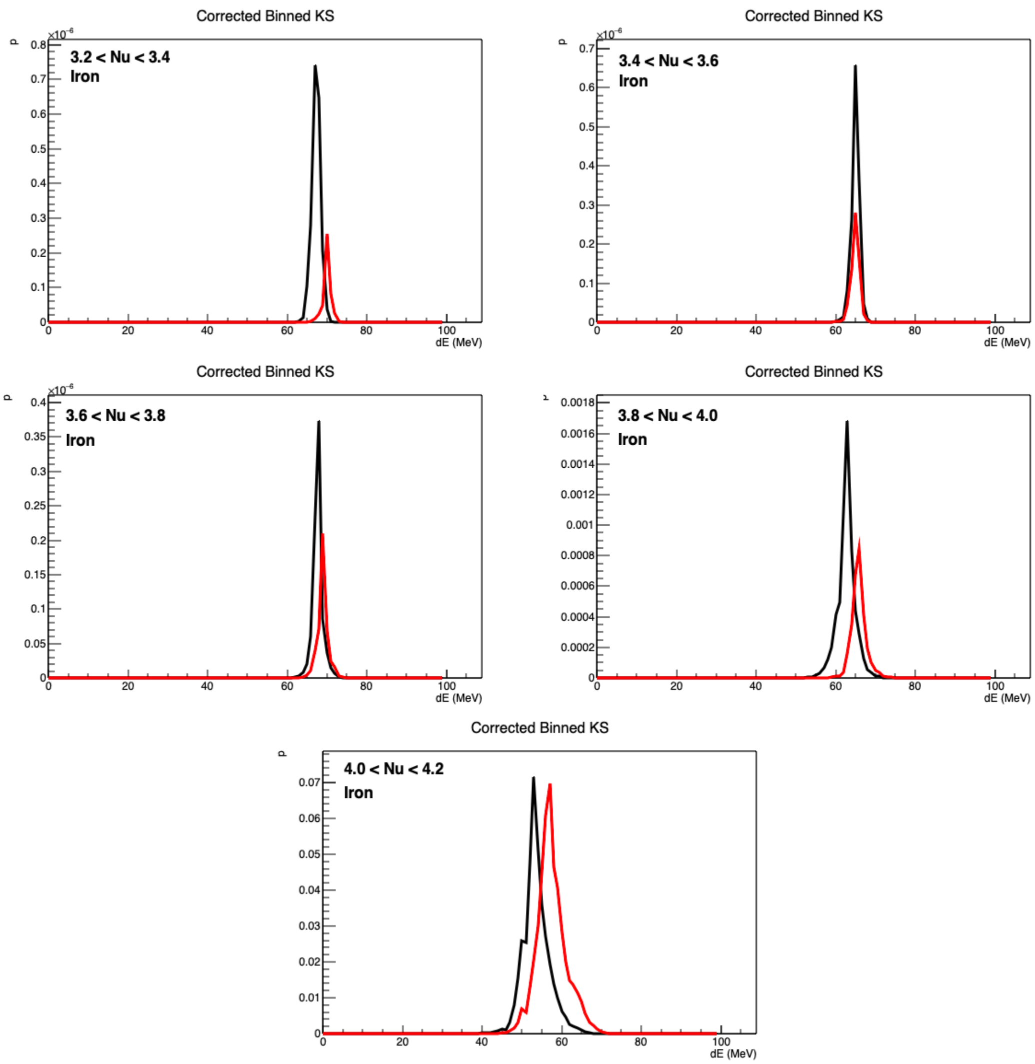

Figure 4.14: Probability values of binned KS-test for the iron target as a function of the energy shift. The black and red curves are for data corrected with 1D and 2D acceptances, respectively.

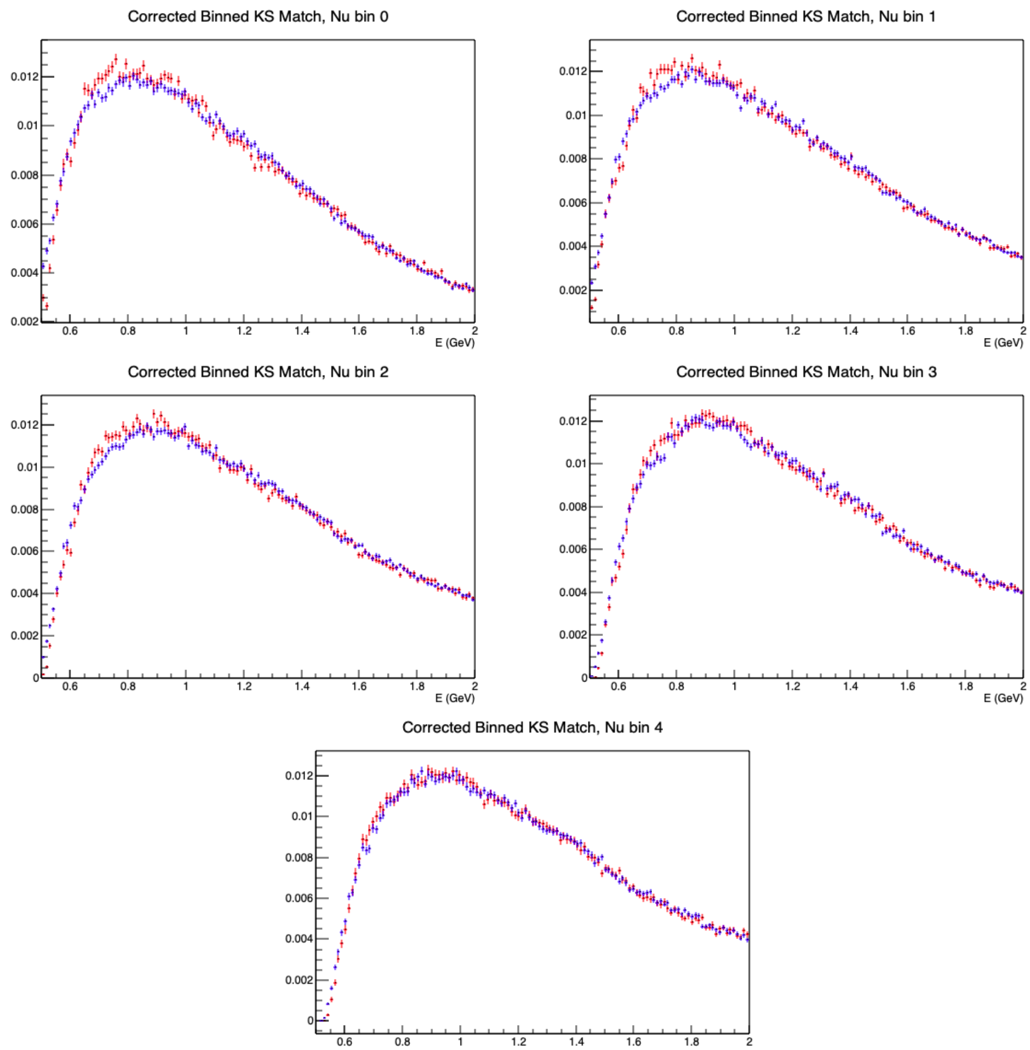

Figure 4.15: Corrected pion energy spectra for deuterium (blue) superimposed on the pion energy spectrum for iron (red) which has been shifted horizontally along the axis by the measured energy loss. The data are normalized to unity for comparison and have 2D acceptance corrections. Error bars represent statistical error only.

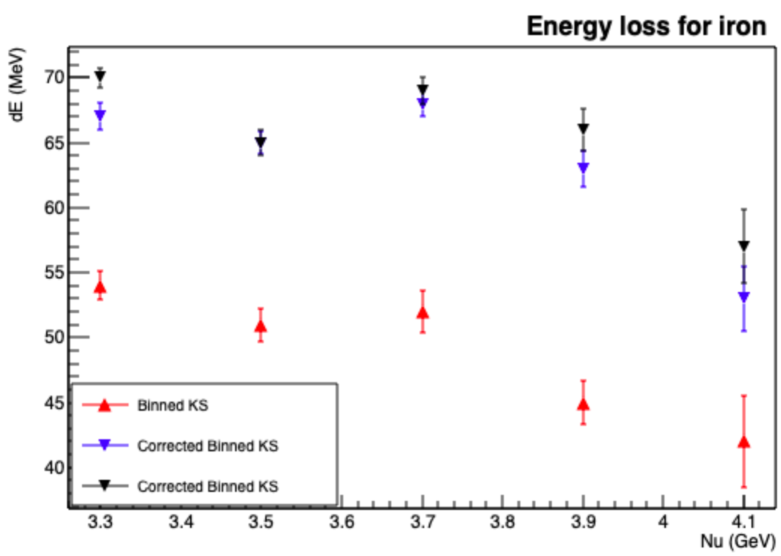

Figure 4.16: Quark energy loss for iron as a function of ν. The red points represent uncorrected results while the blue and black points are for 1D and 2D acceptance corrected data, respectively.

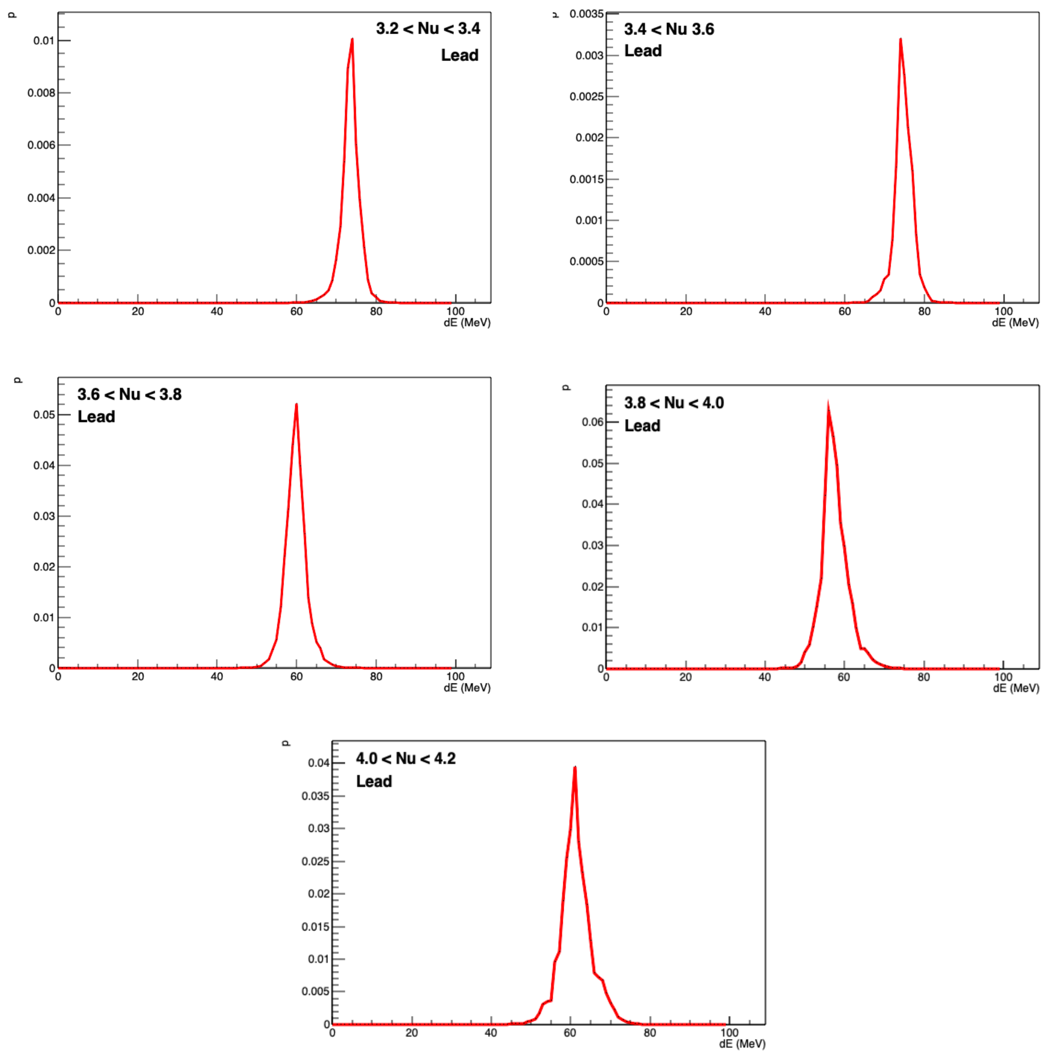

Figure 4.17: Probability values of binned KS-test for the lead target as a function of the energy shift. The plots are for uncorrected data.

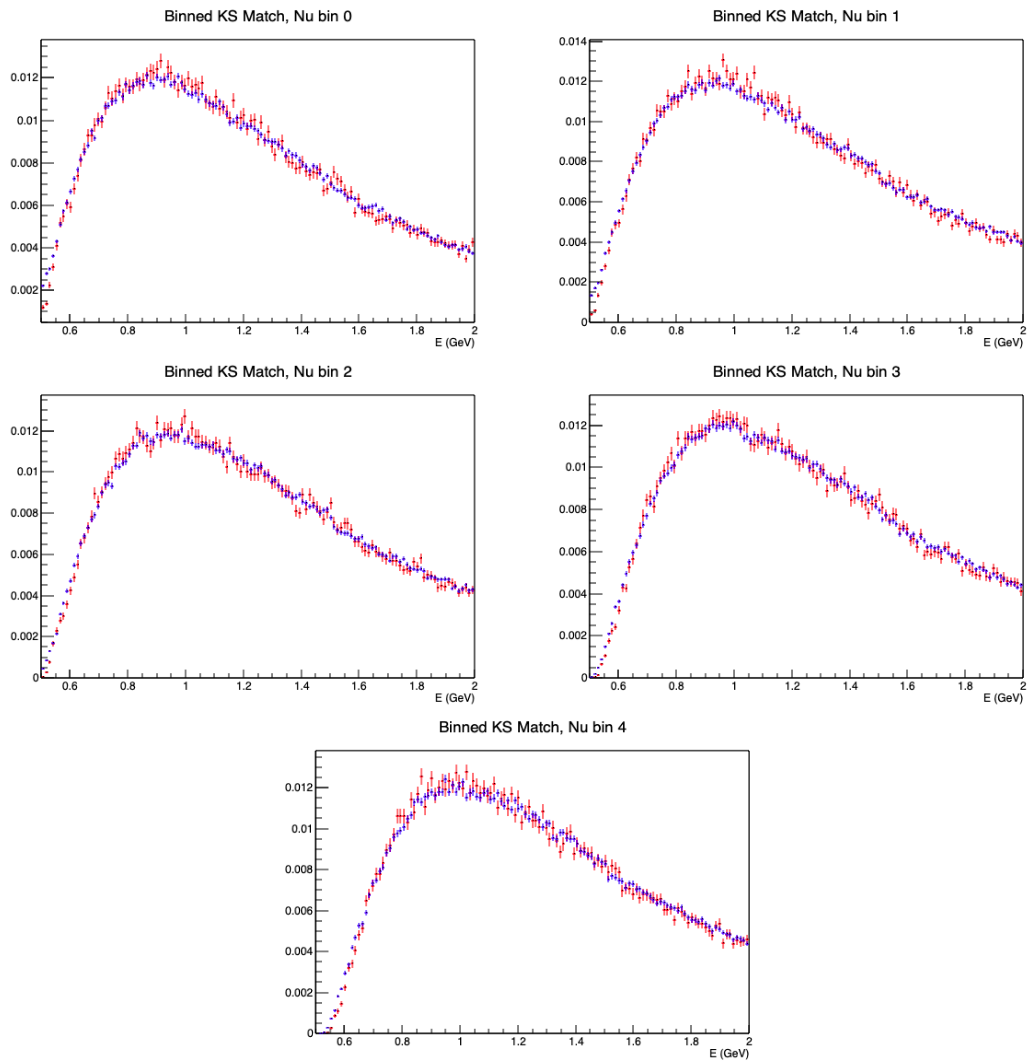

Figure 4.18: Uncorrected pion energy spectra for deuterium (blue) superimposed on the pion energy spectrum for lead (red) which has been shifted horizontally along the axis by the measured energy loss. The data are normalized to unity for comparison and the data have no corrections. Error bars represent statistical error only.

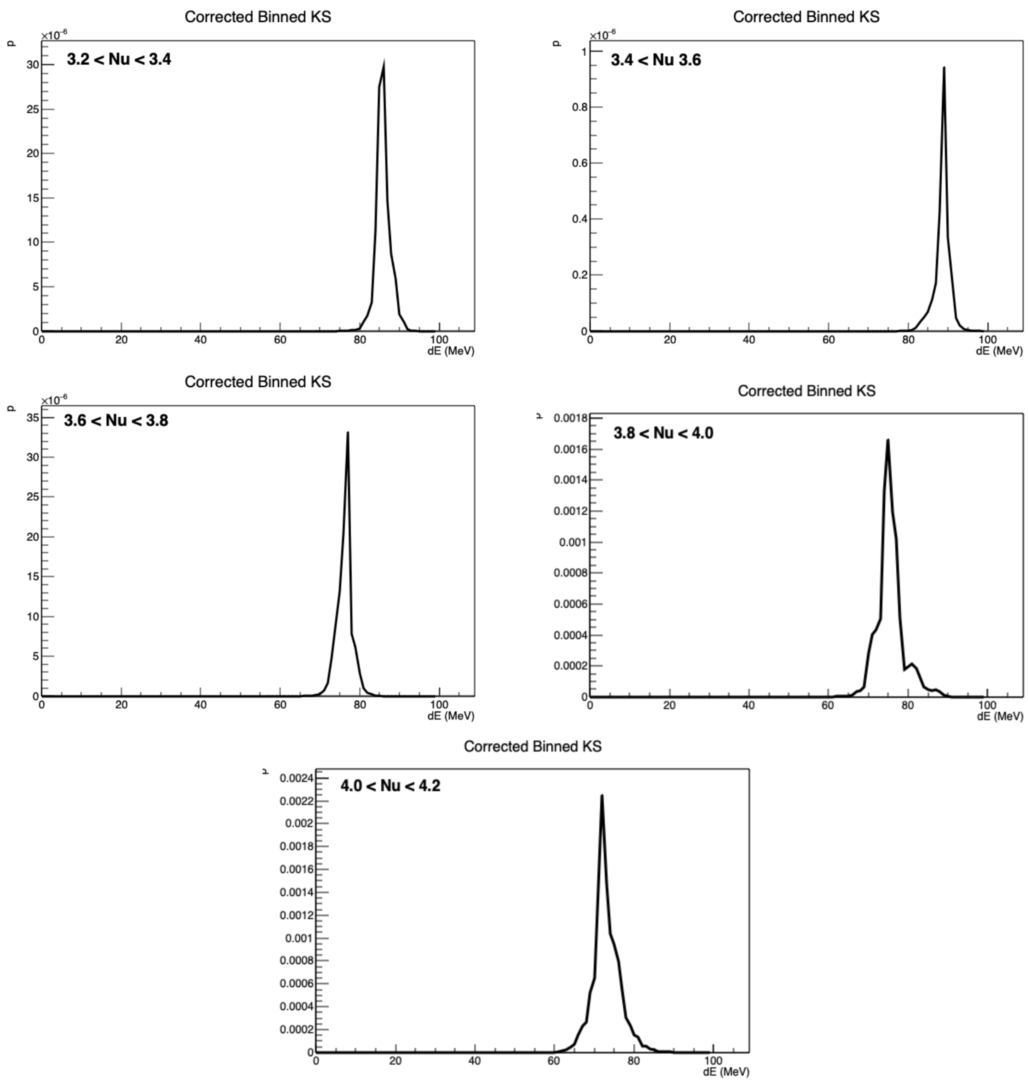

Figure 4.19: Probability values of binned KS-test for the lead target as a function of the energy shift. The plots are for 1D acceptance corrected data.

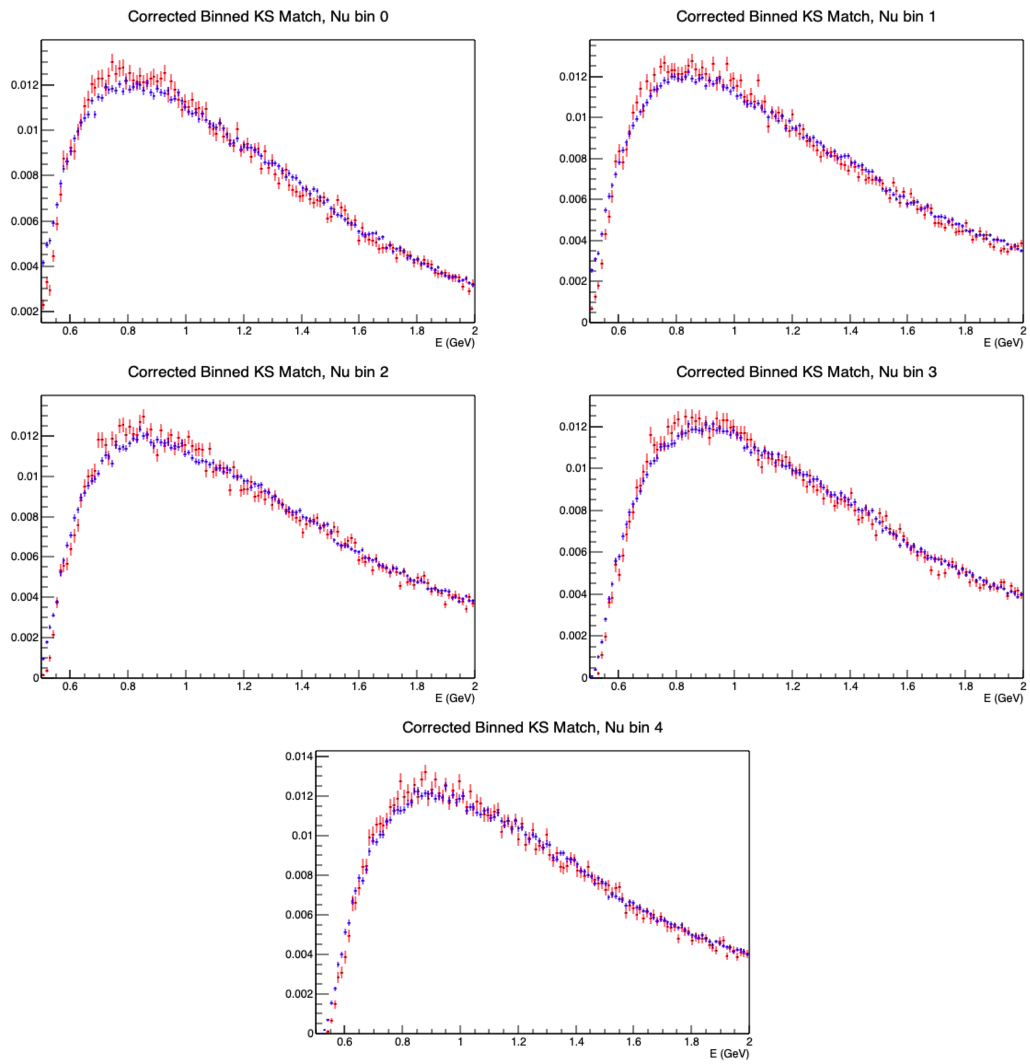

Figure 4.20: Corrected pion energy spectra for deuterium (blue) superimposed on the pion energy spectrum for lead (red) which has been shifted horizontally along the axis by the measured energy loss. The data are normalized to unity for comparison and the data have 1D acceptance corrections. Error bars represent statistical error only.

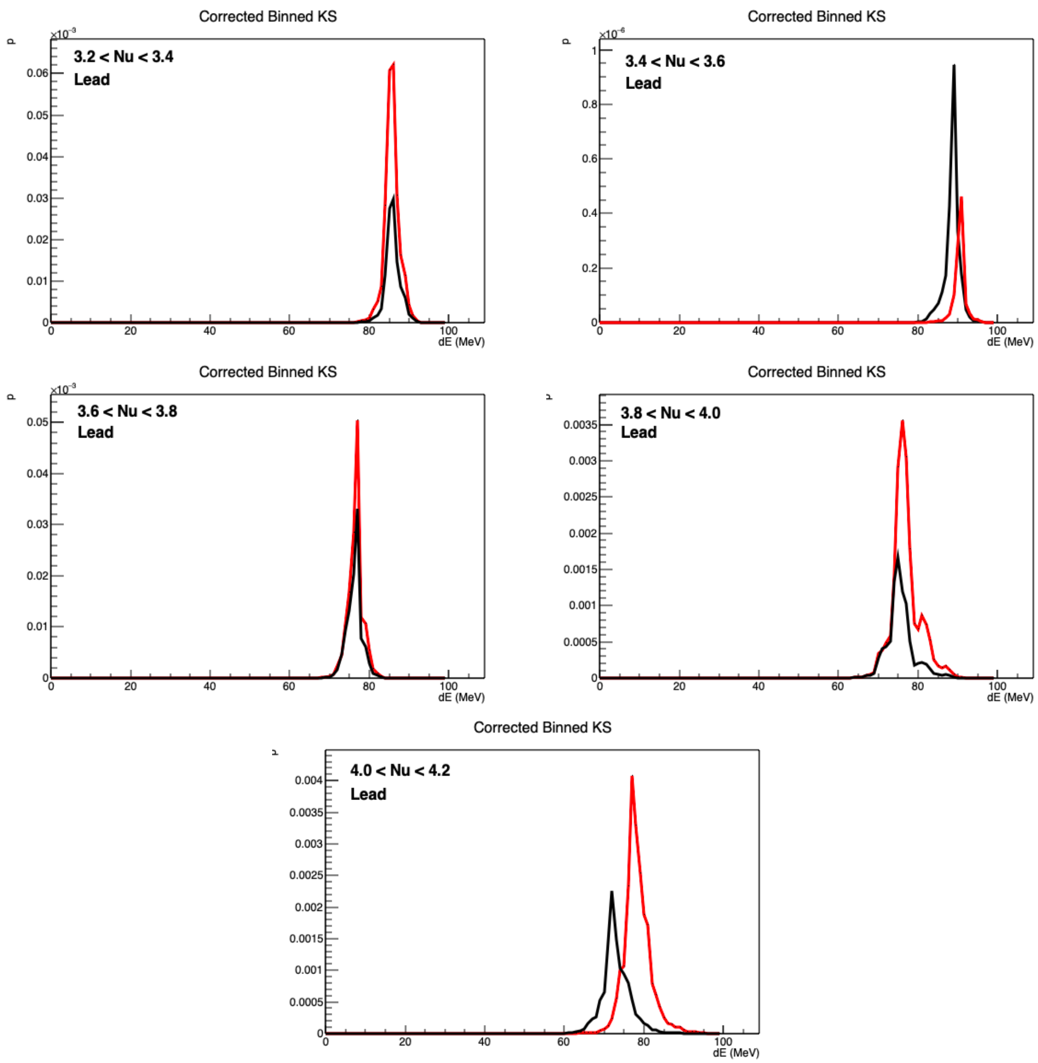

Figure 4.21: Probability values of binned KS-test for the lead target as a function of the energy shift. The red curves are for 2D acceptances while the black curves are for 1D.

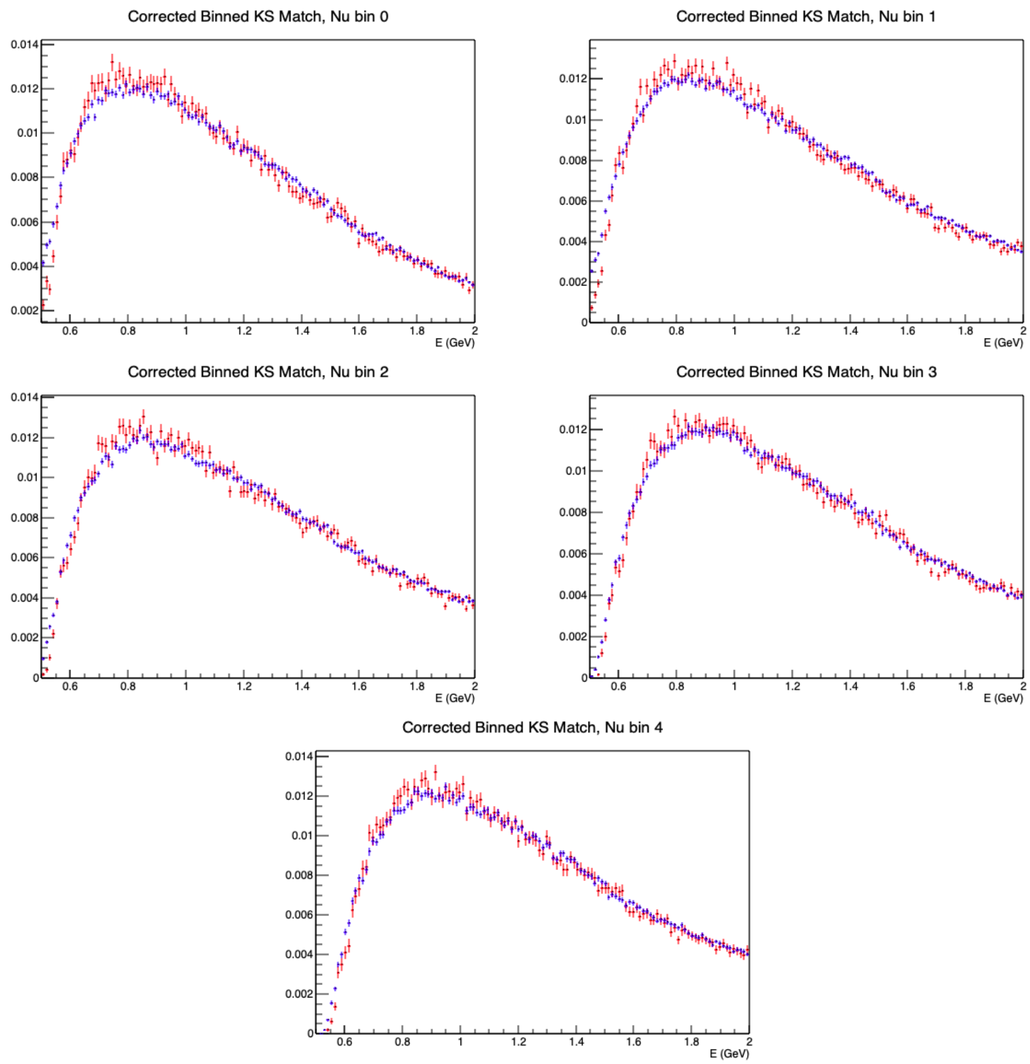

Figure 4.22: Corrected pion energy spectra for deuterium (blue) superimposed on the pion energy spectrum for lead (red) which has been shifted horizontally along the axis by the measured energy loss. The data are normalized to unity for comparison and the data have 2D acceptance corrections. Error bars represent statistical error only.

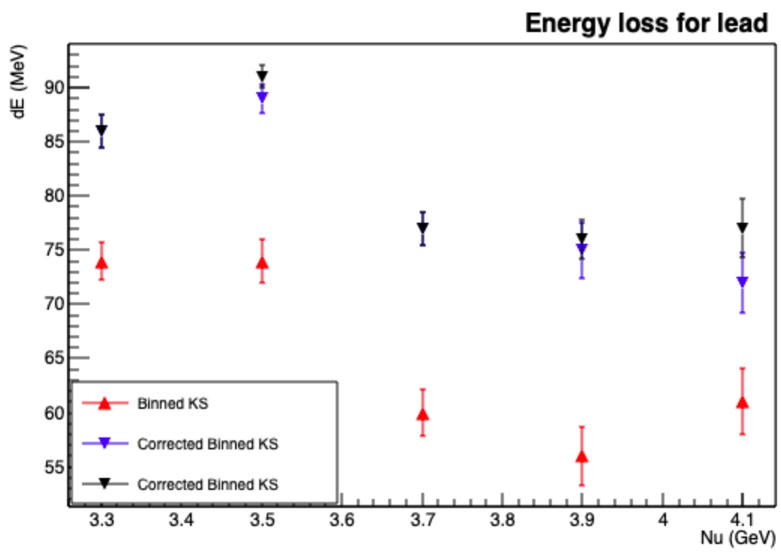

Figure 4.23: Quark energy loss of the lead target as a function of ν. Red is for uncorrected data, blue and black are for 1D and 2D acceptance corrected respectively.

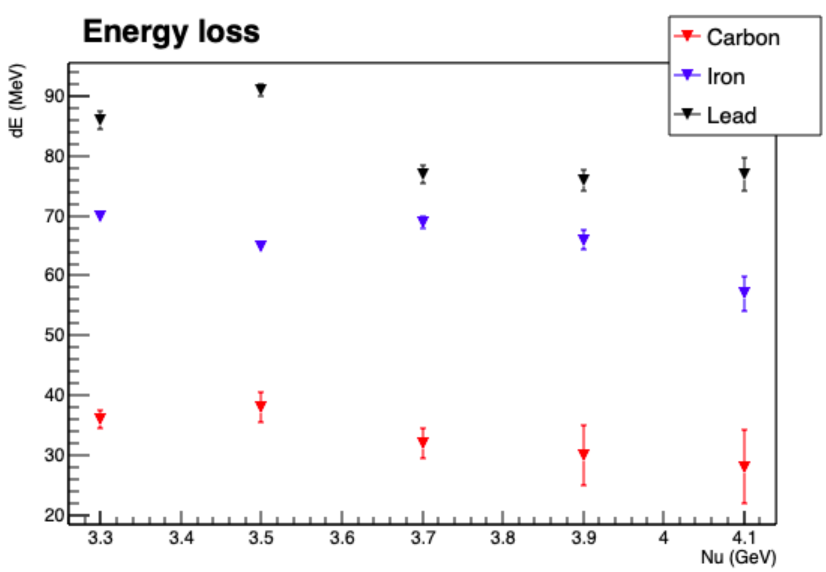

Figure 4.24: Quark energy loss as a function of ν for all targets and 2D acceptance corrected data (without Coulomb corrections).

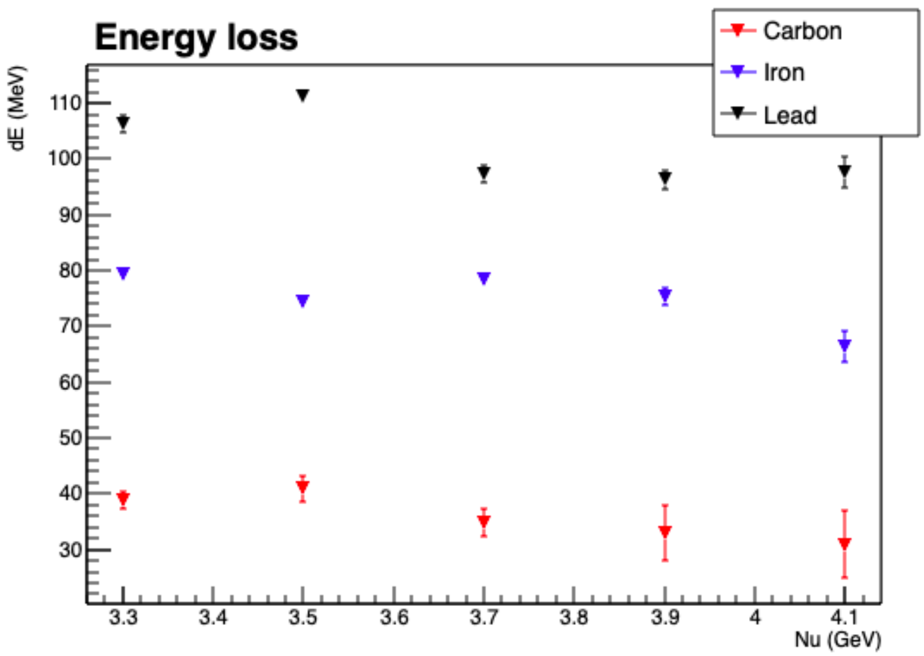

Figure 4.25: Quark energy loss as a function of ν for all targets and 2D acceptance corrected data and Coulomb corrections from Table 3.1

Chapter 5

Conclusions and Future Analysis

With this analysis it was possible to observe the difference in energy loss for the different nucleus sizes. It was observed that this energy loss is larger for bigger nuclei. Besides, the effect of the acceptance corrections has been shown to be important. The ν-dependance expected is approximately observed, but a slight downward trend with ν is systematic for all three nuclei.

For the future, the acceptance corrections should be taken forward, differentiating for more variables, as long as there is enough statistics. There are also more corrections to be made: a proper calculation of Coulomb corrections and radiative corrections are of extreme importance.

Bibliography

[1] J.J. Thomson. “Cathode Rays”. In: *The London, Edinburgh, and Dublin Philosophical Magazine and Journal of Science* 44.269 (1897), pp. 293–316. DOI: 10.1080/14786449708621070. URL: https://doi.org/10.1080/14786449708621070.

[2] N. Bohr. “I. On the constitution of atoms and molecules”. In: *The London, Edin- burgh, and Dublin Philosophical Magazine and Journal of Science* 26.151 (1913), pp. 1–25. DOI: 10.1080/14786441308634955. URL: https://doi.org/10.1080/14786441308634955.

[3] M. Gell-Mann. “A schematic model of baryons and mesons”. In: *Physics Letters* 8.3 (1964), pp. 214–215. ISSN: 1476-4687. DOI: https://doi.org/10.1016/S0031-9163(64)92001-3. URL: http://www.sciencedirect.com/science/article/pii/S0031916364920013.

[4] G Zweig. “An SU_3 model for strong interaction symmetry and its breaking; Version 2”. In: (1964). Version 1 is CERN preprint 8182/TH.401, Jan. 17, 1964, 80 p. URL: https://cds.cern.ch/record/570209.

[5] Richard P. Feynman. “The Behavior of Hadron Collisions at Extreme Energies”. In: *Special Relativity and Quantum Theory: A Collection of Papers on the Poincaré Group*. Ed. by M. E. Noz and Y. S. Kim. Dordrecht: Springer Netherlands, 1988, pp. 289–304. ISBN: 978-94-009-3051-3. DOI: 10.1007/978-94-009-3051-3_25. URL: https://doi.org/10.1007/978-94-009-3051-3_25.

[6] Bo Andersson et al. "Parton Fragmentation and String Dynamics". In: *Phys. Rept.* 97 (1983), pp. 31–145. DOI: 10.1016/0370-1573(83)90080-7.

[7] Torbjörn Sjöstrand et al. "An introduction to PYTHIA 8.2". In: *Comput. Phys. Commun.* 191 (2015), pp. 159–177. DOI: 10.1016/j.cpc.2015.01.024. arXiv: 1410.3012 [hep-ph].

[8] R. Baier, D. Schiff, and B. G. Zakharov. "Energy Loss in Perturbative QCD". In: *Annual Review of Nuclear and Particle Science* 50.1 (2000), 37–69. ISSN: 1545-4134. DOI: 10.1146/annurev.nucl.50.1.37. URL: http://dx.doi.org/10.1146/annurev.nucl.50.1.37.

[9] Yuri L. Dokshitzer et al. *Basics of perturbative QCD*. 1991.

[10] Oscar Andrés Aravena Ortega. "Parton energy loss estimates using positive pions in DIS on nuclear targets (CLAS EG2-Experiment)". PhD thesis. Universidad Tecnica Federico Santa Maria, 2017.

[11] B.A. Mecking et al. "The CEBAF large acceptance spectrometer (CLAS)". In: *Nuclear Instruments and Methods in Physics Research Section A: Accelerators, Spectrometers, Detectors and Associated Equipment* 503.3 (2003), pp. 513 – 553. ISSN: 0168-9002. DOI: https://doi.org/10.1016/S0168-9002(03)01001-5. URL: http://www.sciencedirect.com/science/article/pii/S0168900203010015.

[12] M.D Mestayer et al. "The CLAS drift chamber system". In: *Nuclear Instruments and Methods in Physics Research Section A: Accelerators, Spectrometers, Detectors and Associated Equipment* 449.1 (2000), pp. 81 –111. ISSN: 0168-9002. DOI: https://doi.org/10.1016/S0168-9002(00)00151-0. URL: http://www.sciencedirect.com/science/article/pii/S0168900200001510.

[13] Hayk Hakobyan. "Observation of Quark Propagation Pattern in Nuclear Medium". PhD thesis. Yerevan State University, 2008.

[14] G. Adams et al. “The CLAS Cherenkov detector”. In: *Nuclear Instruments and Methods in Physics Research Section A: Accelerators, Spectrometers, Detectors and Associated Equipment* 465.2 (2001), pp. 414–427. ISSN: 0168-9002. DOI: https://doi.org/10.1016/S0168-9002(00)01313-9. URL: https://www.sciencedirect.com/science/article/pii/S0168900200013139.

[15] E.S. Smith et al. “The time-of-flight system for CLAS”. In: *Nuclear Instruments and Methods in Physics Research Section A: Accelerators, Spectrometers, Detectors and Associated Equipment* 432.2 (1999), pp. 265–298. ISSN: 0168-9002. DOI: https://doi.org/10.1016/S0168-9002(99)00484-2. URL: https://www.sciencedirect.com/science/article/pii/S0168900299004842.

[16] M. Amarian et al. “The CLAS forward electromagnetic calorimeter”. In: *Nuclear Instruments and Methods in Physics Research Section A: Accelerators, Spectrometers, Detectors and Associated Equipment* 460.2 (2001), pp. 239–265. ISSN: 0168-9002. DOI: https://doi.org/10.1016/S0168-9002(00)00996-7. URL: https://www.sciencedirect.com/science/article/pii/S0168900200009967.

[17] H. Hakobyan et al. “A double-target system for precision measurements of nuclear medium effects”. In: *Nuclear Instruments and Methods in Physics Research Section A: Accelerators, Spectrometers, Detectors and Associated Equipment* 592.3 (2008), pp. 218 –223. ISSN: 0168-9002. DOI: https://doi.org/10.1016/j.nima.2008.04.055. URL: http://www.sciencedirect.com/science/article/pii/S0168900208006098.

[18] R. Brun and F. Rademakers. “ROOT: An object oriented data analysis framework”. In: *Nucl. Instrum. Meth.* A389 (1997), pp. 81–86. DOI: 10.1016/S0168-9002(97)00048-X.

[19] *Analyser*. URL: https://github.com/utfsm-eg2-data-analysis/Analyser.

[20] Sebastián Morán Vásquez. “Study of Hadronization Process using Positive Pions with CLAS in Jefferson Lab”. PhD thesis. Universidad Técnica Federico Santa María, 2021.

[21] Barak Schmookler. “Nucleon Structure and Its Modification in Nuclei”. PhD thesis. MASSACHUSETTS INSTITUTE OF TECHNOLOGY, 2018.